Improved Representation of Boundary Layer Clouds over the Southeast Pacific in ARW-WRF Using a Modified Tiedtke Cumulus Parameterization Scheme*

CHUNXI ZHANG, YUQING WANG, AND KEVIN HAMILTON

International Pacific Research Center, and Department of Meteorology, School of Ocean and Earth Science and Technology, University of Hawaii at Manoa, Honolulu, Hawaii

(Manuscript received 6 December 2010, in final form 15 April 2011)

ABSTRACT

A modified Tiedtke cumulus parameterization (CP) scheme has been implemented into the Advanced Research Weather Research and Forecasting model (ARW-WRF) to improve the representation of marine boundary layer (MBL) clouds over the southeast Pacific (SEP). A full month simulation for October 2006 was performed by using the National Centers for Environmental Prediction (NCEP) final analysis (FNL) as both the initial and lateral boundary conditions and the observed sea surface temperature (SST). The model simulation was compared with satellite observations and with results from an intense ship-based campaign of balloon soundings during 16–20 October 2006 at 20°S, 85°W.

The model with the modified Tiedtke scheme successfully captured the main features of the MBL structure and low clouds over the SEP, including the geographical distribution of MBL clouds, the cloud regime transition, and the vertical structure of the MBL. The model simulation was repeated with the various CP schemes currently provided as standard options in ARW-WRF. The simulations with other CP schemes failed to reproduce the geographical distribution of cloud fraction and the observed cloud regime transition, and displayed an MBL too shallow compared to observations. The improved simulation with the modified Tiedtke scheme can be attributed to a more active parameterized shallow convection with the modified Tiedtke scheme than with the other CP schemes tested, which played a critical role in lifting the inversion base and the low cloud layer. Results from additional sensitivity experiments employing different planetary boundary layer (PBL) parameterization schemes demonstrated that the basic feature of the MBL structure and low clouds over the SEP were not particularly sensitive to the choice of the PBL scheme.

1. Introduction

The persistent boundary layer cloud deck over the southeast Pacific (SEP) is an important aspect of the global climate system. This cloud deck is mainly a result of the large-scale subsidence in subtropical oceans and coastal upwelling-induced cold sea surface temperature (SST), both favoring the formation of a low-level temperature inversion and boundary layer clouds (Bretherton et al. 2004; Wang et al. 2004a). These boundary layer clouds are dominated by stratus off the west coast of South America and then stratocumulus offshore and finally trade cumuli farther to the west in response to the westward increase in SST. In particular, both stratus and stratocumulus clouds form at the top of the marine boundary layer (MBL) under a sharp inversion of temperature and moisture (Klein and Hartmann 1993).

These MBL clouds play an important role in the energy balance both at the earth surface and at the top of the atmosphere. A realistic representation of these clouds in climate models is crucial for accurate climate simulations (Hannay et al. 2009). Unfortunately these MBL clouds are still poorly simulated in most of the current state-of-the-art regional and global climate models (e.g., Hannay et al. 2009; Wyant et al. 2010). Common discrepancies include an erroneous spatial distribution of clouds and a too shallow boundary layer depth (Wyant et al. 2010). Some earlier studies have shown that the treatments of shallow convection and subgrid vertical mixing are key to the

* School of Ocean and Earth Science and Technology Publication Number SOEST-8141 and the International Pacific Research Center Publication Number IPRC-778.

Corresponding author address: Dr. Yuqing Wang, International Pacific Research Center, SOEST, University of Hawaii at Manoa, 1680 East-West Rd., Honolulu, HI 96822.
E-mail: yuqing@hawaii.edu

DOI: 10.1175/MWR-D-10-05091.1

representation of MBL clouds in climate models (e.g., Siebesma and Cuijpers 1995; Bretherton et al. 2004; McCaa and Bretherton 2004; Wang et al. 2004a,b; Park and Bretherton 2009).

A cumulus parameterization (CP) scheme must estimate the rate of subgrid-scale convective precipitation, release of latent heat, and the redistribution of heat, moisture, and momentum in the vertical due to convection (Kain and Fritsch 1990). Cumulus convection modifies the large-scale temperature and moisture fields through detrainment and cumulus-induced subsidence in the environment. The detrainment causes large-scale cooling and moistening, and the cumulus-induced subsidence causes large-scale warming and drying (Arakawa and Schubert 1974). Many results show the importance of the coexistence of shallow clouds and deep clouds in maintaining the large-scale heat and moisture budgets (Yanai et al. 1973; Arakawa and Schubert 1974; Betts 1986). Shallow convection produces a kind of cumulus cloud that is not deep enough for precipitation processes. By transporting air from the surface mixed layer to the lower free troposphere, shallow convection strongly influences boundary layer depth, temperature, moisture, cloud cover, and winds (Bretherton et al. 2004; Kain 2004; Wang et al. 2004a,b; de Szoeke et al. 2006).

Because boundary layer clouds interact strongly with turbulence in the planetary boundary layer (PBL), accurate representation of the PBL in an atmospheric model is also critical to successful simulations of MBL clouds (Randall et al. 1985; McCaa and Bretherton 2004; Wang et al. 2004a,b). The vertical transport of heat and moisture in the boundary layer by the PBL scheme together with a shallow convection scheme mainly accounts for the position and intensity of MBL clouds (Bretherton et al. 2004). The coupling between the shallow cumulus scheme and the PBL scheme is the model representation of the physical interaction among surface fluxes, the boundary layer structure, and MBL clouds and this coupling is thought to be significant (Bretherton et al. 2004). Observations of the statistical similarity of the subcloud mixed layer to a dry convective boundary layer that is not overlain by cumuli (Siebesma et al. 2003) support an assumption that cumulus updrafts do not affect the turbulent structure of the PBL beneath them, but when cumuli exist at the top of the PBL, the interaction between the cloud base and the PBL top becomes more complicated (Bretherton et al. 2004).

The Advanced Research Weather Research and Forecasting model (ARW-WRF) is the new-generation model for both weather research and forecasting (Skamarock et al. 2008), and is also widely used for regional climate research (Leung et al. 2006; Bukovsky and Karoly 2009; Awan et al. 2011). In general, at least some standard versions of the current ARW-WRF model when applied to the SEP produce a much shallower boundary layer than observed and also displays amplitude and phase errors in the diurnal cycle of liquid water path (LWP) compared to observations (Wyant et al. 2010). Here at the International Pacific Research Center (IPRC) we have developed the IPRC regional atmospheric model (iRAM) and shown that the cloud and boundary layer simulations over the SEP are rather realistic (Wang et al. 2003, 2004a,b, 2005; Wyant et al. 2010). It is likely that the good simulation is attributable to the modified Tiedtke CP scheme in iRAM, which takes into account penetrative, middle, and shallow convections (Tiedtke 1989; Nordeng 1995; Wang et al. 2003, 2004a). We have recently implemented the iRAM CP scheme into the ARW-WRF model (V3.2.1) at IPRC with the goal of improving the overall simulation of MBL clouds, thus making ARW-WRF suitable for regional climate studies over the subtropical oceans.

The objectives of this paper are 1) to document the implementation of the modified Tiedtke CP scheme into the ARW-WRF model, 2) to examine the skill of the modified WRF model in simulating the MBL structure and low clouds over the SEP, and 3) to understand the reason why the Tiedtke scheme performs better than other CP schemes over the SEP. We will show results from two sets of numerical experiments. In set A, we keep a single PBL scheme and intercompare simulations with different CP schemes, including the newly implemented modified Tiedtke scheme and the schemes currently available in ARW-WRF. In set B, we examined the sensitivity of the simulation of the version with the newly implemented Tiedtke scheme to incorporation of different PBL schemes. We focus on the subtropical region off the west coast of South America and consider the month of October 2006, the same period as that simulated in the Preliminary Variability of the American Monsoon Systems (VAMOS) Ocean–Cloud–Atmosphere–Land Study (VOCALS) model Assessment (PreVOCA) project (Wyant et al. 2010). The model simulations were verified by using satellite remote sensing data, reanalysis data, and the ship-based observations from the National Oceanic and Atmospheric Administration (NOAA) and the Woods Hole Oceanographic Institution (WHOI) cruises to the stratus buoy (20°S, 85°W).

Section 2 describes the implementation of the modified Tiedtke CP scheme into the ARW-WRF model, the model configuration, and the observational datasets used in model verification. Results from the intercomparison among different CP schemes and observations are discussed in section 3. Section 4 examines the sensitivity of the simulated MBL structure and low clouds using the

Tiedtke scheme to different PBL schemes. A summary is given in the last section. Different CP schemes and PBL schemes tested in this study are briefly described in appendixes A and B, respectively.

2. Model and data descriptions

a. The modified Tiedtke scheme

Compared to the original Tiedtke CP scheme (Tiedtke 1989), the scheme used here has been modified in several respects (Nordeng 1995; Wang et al. 2003, 2004a, 2007). This modified Tiedtke scheme uses a convective available potential energy (CAPE) closure instead of the original moisture convergence closure and considers the organized entrainment and detrainment based on a simple cloud plume model (Nordeng 1995). In the original Tiedtke scheme, the organized entrainment is consistent with the closure and is based on a moisture convergence hypothesis under static conditions (Tiedtke 1989). Here, the organized entrainment is assumed to take place as organized inflow of air into the cloud when cloud parcels accelerate upward and the buoyancy is positive. The organized detrainment takes place where the air decelerates when the buoyancy is negative.

In addition to the organized entrainment and detrainment, the turbulent entrainment and detrainment are also included. The turbulent entrainment and detrainment rates are considered to be the same so that they do not contribute to the change of mass flux with height. The fractional turbulent entrainment–detrainment rate ε^T/δ^T depends inversely on the radius of the ensemble cloud base R (Simpson 1971):

$$\varepsilon^T = \delta^T = \frac{0.2}{R}. \tag{1}$$

Tiedtke (1989) assumed the entrainment–detrainment rates to be 1×10^{-4} m^{-1} for penetrative deep convection and 3×10^{-4} m^{-1} for shallow convection. Wang et al. (2004a, 2007) showed that this entrainment–detrainment rate for shallow convection was too small and generally resulted in an underestimation of boundary layer clouds due to too active shallow convection. They noted that a fractional turbulent entrainment–detrainment rate of as high as 2×10^{-3} m^{-1} for shallow convection could be justified based on earlier large-eddy simulation results (Siebesma and Holtslag 1996). Wang et al. (2007) also demonstrated that increasing the entrainment–detrainment rates for either deep or shallow convection in the Tiedtke scheme would prolong the development and reduce the strength of deep convection, thus reducing bias in the simulated precipitation diurnal cycle. In our current implementation in the WRF model, we have set the entrainment–detrainment rate to 1×10^{-4} m^{-1} for penetrative deep convection and 1.2×10^{-3} m^{-1} for shallow convection.

To improve the simulation of MBL clouds, Wang et al. (2004a,b) also adjusted the fraction of the cloud ensemble of shallow convection that penetrates into the inversion layer and detrains there into the environment. They found that the original value of 0.33 used in Tiedtke (1989) was too large and produced much less boundary layer clouds due to the fact that too much cloud water would be detrained across the inversion base and evaporate there. In our current implementation in the WRF model, we reduced the fraction to 0.26, which is close to that (0.23) used in Wang et al. (2004a,b) in their iRAM simulations of the SEP.

Another modification to the original Tiedtke scheme is the treatment of the detrained cloud condensates at the top of cumulus towers, which evaporated immediately in the original scheme (Tiedtke 1989) but are returned to the grid-scale cloud water/ice as in Roeckner et al. (1996). The probability functions f_{liq} and f_{ics} derived by Rockel et al. (1991) were used to partition between cloud water and cloud ice the detrained condensates above the freezing level ($T < T_0 = 273.15$ K with T being the ambient air temperature). The liquid and ice fractions are given by

$$f_{\text{liq}} = a + (1 - a)e^{-b(T-T_0)^2}, \quad f_{\text{ice}} = 1 - f_{\text{liq}}, \tag{2}$$

where $a = 0.0059$, and $b = 0.003\,102$, while $f_{\text{liq}} = 1$ for $T \geq T_0$.

In addition, to prevent deep convection occurring in dry regions, a threshold value RH_c is set for the vertically averaged relative humidity $\overline{\text{RH}}$ between the detected cloud top and cloud base. Deep convection is allowed to occur only when $\overline{\text{RH}} \geq \text{RH}_c$ (=0.8 in our new version of the ARW-WRF).

b. Model configuration

The ARW-WRF version 3.2.1 (Skamarock et al. 2008) was configured for a single domain (Fig. 1) with 27-km horizontal resolution and 31 full terrain-following σ levels in the vertical (14 levels below 700 hPa with the model top at 50 hPa). There are 320 grid points in the east–west direction and 300 grid points in the north–south direction. The shortwave and longwave radiation fluxes are calculated based on the Community Atmospheric Model, version 3 (CAM3; Collins et al. 2004). Cloud fraction is diagnosed based on grid-scale cloud ice and cloud water mixing ratios and the value is between 0 and 1 fraction (Xu and Randall 1996; Hong et al. 1998). The WRF Single-Moment 6-Class Microphysics scheme (WSM6) microphysics scheme is used for grid-scale cloud and precipitation processes (Hong and Lim). The Noah land surface model is used for the land surface processes

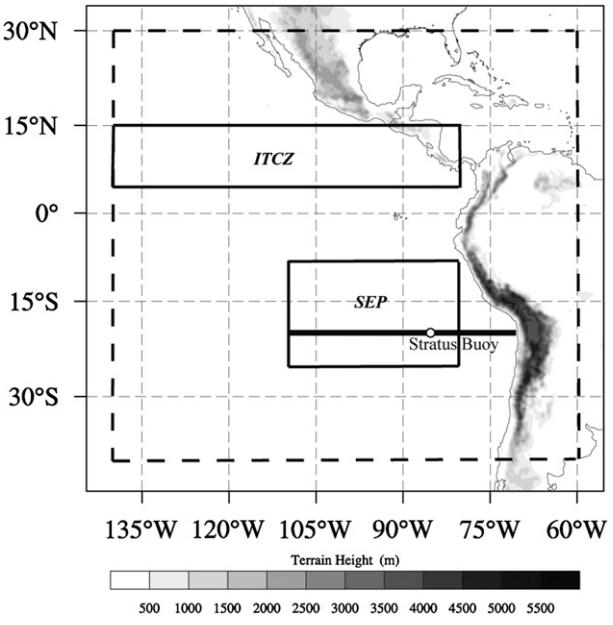

FIG. 1. The ARW-WRF model domain and model representation of the topography contoured with contour interval of 500 m. The thick dashed rectangle shows the inner domain used in the analysis. The thick solid line is for the vertical cross-section plot in Fig. 10. The ''stratus buoy'' is at 20°S, 85°W. The solid rectangles are the ITCZ region and SEP region, respectively.

(Chen and Dudhia 2001). The standard gravity wave drag parameterization is employed in all simulations discussed here (Kim and Arakawa 1995).

The CP and PBL schemes tested in this study are listed in Tables 1 and 2 and briefly described in appendixes A and B, respectively. We chose the Yonsei University (YSU) PBL scheme in the experiments to intercompare different CP schemes, including the Tiedtke scheme (TDK), the Kain–Fritsch scheme (KFETA), the Betts–Miller–Janjić scheme (BMJ), and the Simplified Arakawa–Schubert scheme (SAS). Results are discussed in section 3. Four additional experiments were performed to examine the sensitivity of the simulation with the TDK CP scheme to different PBL schemes, including the Asymmetric Convective Model (ACM2), the Mellor–Yamada–Janjić (MYJ), the Mellor–Yamada–Nakanishi–Niino (MYNN), and the Bougeault–Lacarrere (BouLac) schemes. Results are discussed in section 4.

The model initial and lateral boundary conditions in all experiments were obtained from the National Centers for Environmental Prediction (NCEP) final analysis (FNL), which has a horizontal resolution of 1° by 1° on 26 pressure levels at 6-h intervals. The SST is given and updated daily using the 0.5° by 0.5° RGT_SST analysis data (available online at http://polar.ncep.noaa.gov/sst/oper/Welcome.html). The model was initialized at 0000 UTC 1 October 2006 and integrated for a full month. The analysis of results employed 3-hourly model outputs.

c. Data

In addition to the NCEP FNL analysis atmospheric variables, we also used some other datasets to verify the model simulations. Cloud fraction retrieved from the Moderate Resolution Imaging Spectroradiometer (MODIS) was used for cloud fraction verification. The MODIS cloud fraction is based on liquid water retrieval and mostly represents low clouds. The monthly mean liquid water path (LWP) dataset used in model verification was taken from the University of Wisconsin (UWisc) climatology, which was derived from satellite-based passive microwave observations over the global oceans. The tropical rainfall measuring mission (TRMM) 3B43 data are used as observations.

The monthly mean cloud-base and cloud-top heights were obtained from the cloud layer product of the Cloud-Aerosol Lidar and Infrared Pathfinder Satellite Observation (CALIPSO). CALIPSO was launched on 28 April 2006 and is a two-wavelength (532 and 1064) lidar providing high-resolution vertical profiles of aerosols and clouds. Details on CALIPSO and the algorithms used can be found in Winker et al. (2009). Boundary layer clouds are detected at a resolution of 30 m in the vertical and 333 m in the horizontal. The full-resolution product gives up to five cloud layers per profile as provided by the National Aeronautics and Space Administration (NASA) Langley Atmospheric Science Data Center (ASDC, see online at http://eosweb.larc.nasa.gov/). The highest cloud top below 3 km is considered to be the top of low clouds. We interpolated all available CALIPSO data in October 2006 from the original grid to 2.5° × 2.5° grid cell to compose the monthly mean of October 2006. We note that Brunke et al. (2010) found that the CALIPSO-derived cloud-base heights are usually too low and this needs to be considered when we compare the model simulated cloud base heights with satellite observations.

3. Intercomparison among CP schemes

a. Large-scale circulation and precipitation

The large-scale circulation over the SEP in October 2006 was dominated by the subtropical high (Fig. 2a). Surface southeasterly trade winds of 5–9 m s^{-1} prevail from 25°S to 5°N and southerly winds prevail along the west coast of South America due to the influence of the high Andes (Xu et al. 2005). The precipitation for the month is dominated by the intertropical convergence zone (ITCZ) north of the equator and by synoptic weather disturbances to the southwest of the subtropical high (Fig. 2b).

TABLE 1. List of CP schemes tested in this study (see appendix A and section 2a). Also included are references and comments.

CP schemes	References	Comments
Kain–Fritsch scheme (KFETA)	Kain (2004); Kain and Fritsch (1990, 1993)	The modified version of the Kain–Fritsch scheme uses a simple cloud model with moist updrafts and downdrafts. The closure assumption for shallow convection is based on TKE.
Betts–Miller–Janjić scheme (BMJ)	Janjić (1994, 2000); Betts(1986)	It was derived from the Betts–Miller convective adjustment scheme. The deep convection profiles and the relaxation time depends on cloud efficiency. The shallow convection moisture profile is computed by the requirement that the entropy change be small and nonnegative.
Simplified Arakawa–Schubert scheme (SAS)	Pan and Wu (1995); Tiedtke (1983)	Penetrative convection is simplified to only one cloud type mentioned by Grell (1993). Shallow convection is parameterized as an extension of the vertical diffusion scheme as Tiedtke (1983).
Tiedtke scheme (TDK)	Tiedtke (1989); Nordeng (1995); Gregory et al. (2000)	Mass flux considers organized entrainment–detrainment and turbulence entrainment–detrainment. CAPE closure is used for deep convection. Cloud-top detrainment is the coupler between the subgrid-scale convection and grid-resolved moist processes (Wang et al. 2004a).

The model simulated the large-scale circulation reasonably well regardless which CP scheme was used. The model bias in mean sea level pressure (MSLP) and surface winds are shown for each of the CP schemes in Figs. 2c–f. Overall, the model biases in mean sea level pressure (MSLP) and 10-m winds are the smallest in the experiment with the TDK scheme and relatively large with both the KFETA and BMJ schemes. This is also reflected in the root-mean-square error (RMSE) shown in Table 3 for the monthly mean domain-averaged MSLP, 10-m winds, and 500-hPa height. Note that to focus on the eastern Pacific region, only grids over the ocean in the area of 40°S–30°N, 140°–60°W were taken into account in calculating the area means shown in Table 3. Consistent with the model biases shown in Figs. 2c–f, the RMSEs in all three variables are the smallest in the simulation with the TDK scheme and the largest in the simulation with the KFETA scheme.

Figure 3 shows the vertical profiles of the area-averaged model biases in potential temperature and water vapor mixing ratio in the ITCZ region and in the SEP (see Fig. 1 for the definition of the two regions), respectively. In the ITCZ region, the TDK scheme shows small warm biases around 0–0.8 K below about 10 km and a small cold bias above, so does the BMJ scheme (Fig. 3a). The SAS scheme shows alternating warm–cold–warm–cold bias with absolute values less than 1 K. The KFETA scheme shows warm biases as large as 2.0 K below 5 km and cold biases above. The TDK scheme has a wet bias ($1\ g\ kg^{-1}$) below 2.5 km and a dry bias ($-0.5\ g\ kg^{-1}$) above and the other CP schemes show a wet bias below around 0.5 km and a dry bias throughout the free troposphere above (Fig. 3b). The KFETA scheme shows the largest dry bias above 1.3 km. The wettest low troposphere simulated with the TDK scheme reflects a relatively much deeper well-mixed layer, consistent with active deep convection in the ITCZ. Note that the moisture fields in the ITCZ region in the FNL analysis could be unrealistically dry since there are no in situ observations there.

In the SEP, the TDK scheme shows smallest biases in both potential temperature and water vapor mixing ratio (Figs. 3c,d). The other CP schemes show large warm and

TABLE 2. List of PBL schemes tested in this study available in the ARW-WRF model. Also included are references and comments. All schemes are briefly described in appendix B.

PBL schemes	References	Comments
Yonsei University PBL (YSU)	Hong et al. (2006)	Based on MRF PBL. The momentum diffusivity coefficient is formulated by height of PBL and velocity scale in the mixing layer.
Mellor–Yamada–Janjić (MYJ)	Janjić (1990, 1996, 2002)	Modified Mellor–Yamada level 2.5 turbulence closure model. An upper limit is imposed on the master length scale, which influences the eddy diffusivity coefficient.
Mellor–Yamada–Nakanishi–Niino (MYNN; level 2.5)	Nakanishi and Niino (2004)	TKE-based scheme. The master mixing length is designed to be the shorted length scale among the surface layer length, turbulent length, and buoyancy length.
Bougeault–Lacarrere (BouLac)	Bougeault and Lacarrere (1989)	Eddy diffusivity coefficient is limited in some range.
Asymmetric Convective Model (ACM2)	Pleim (2007a,b)	The nonlocal term is explicitly considered by a transient term.

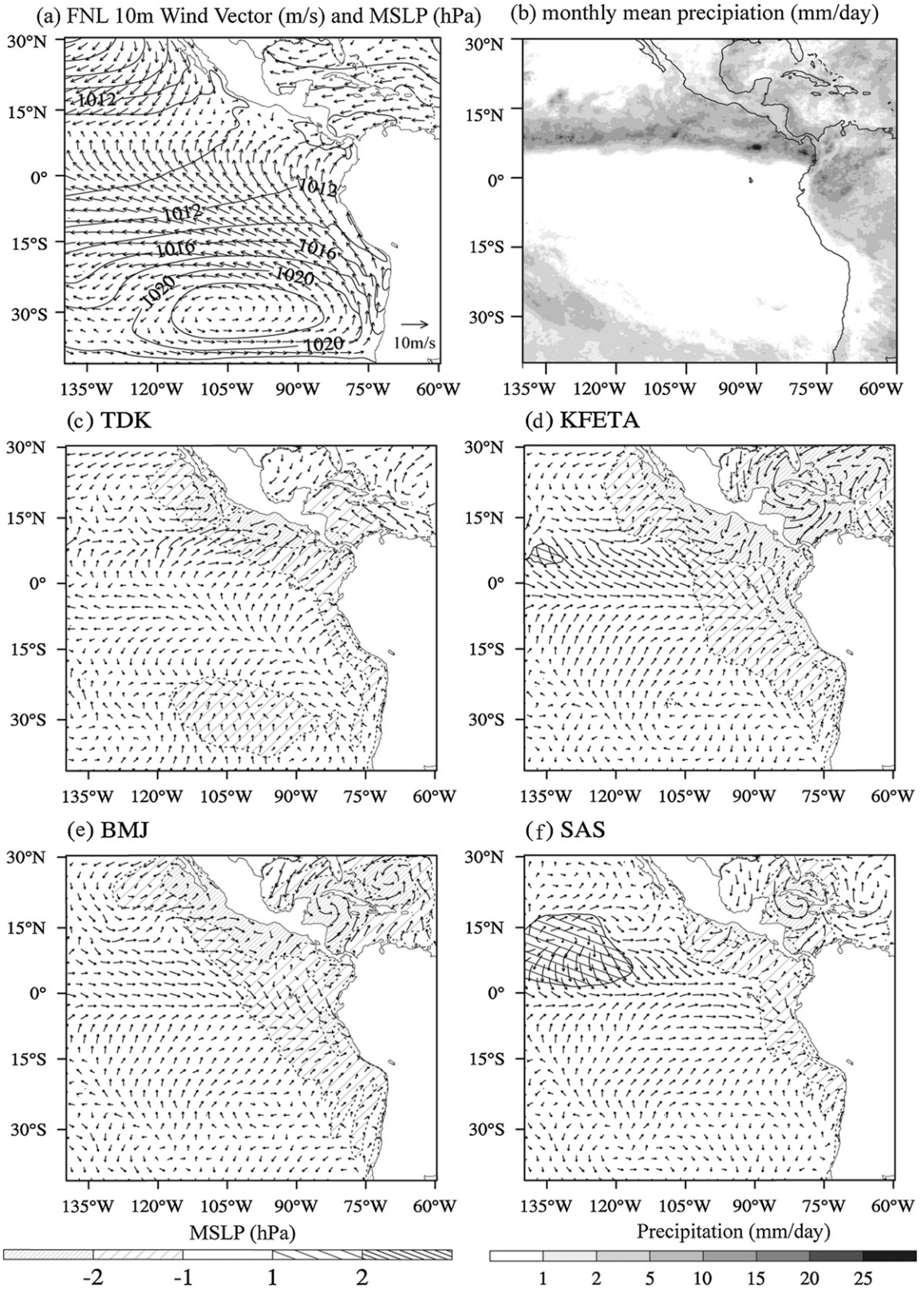

FIG. 2. (a) The monthly mean 10-m winds (m s^{-1}, vectors) and sea level pressure (hPa) from NCEP FNL analysis in October 2006, (b) monthly mean precipitation rate (mm day^{-1}) from TRMM 3B43, and the model biases in monthly mean sea level pressure (hPa, shading). The 10-m winds (m s^{-1}, vectors) from simulations with different CP schemes: (c) TDK, (d) KFETA, (e) BMJ, and (f) SAS.

TABLE 3. Monthly and regional averaged root-mean-square error between the model simulation and NCEP FNL analysis using YSU PBL scheme with different CP schemes as listed in Table 1 and described briefly in appendix A: TDK, KFETA, BMJ, and SAS.

	TDK	KFETA	BMJ	SAS
MSLP (hPa)	0.79	1.50	1.13	0.83
10-m wind speed (m s^{-1})	0.81	1.16	0.81	0.95
500-hPa height (m)	8.60	13.83	10.08	12.55

wet biases in the mid–lower troposphere except for a very shallow surface layer below 0.4 km. Again the KFETA scheme displays the largest biases with a warm bias of 4.7 K and dry bias of 3.7 g kg^{-1} at around 1.5 km. Therefore, both the area-averaged RMSE and vertical profile of model biases suggest that the TDK scheme performed better than other CP schemes available in ARW-WRF model in simulating the large-scale circulation over the eastern Pacific.

During October 2006, significant precipitation was observed both in the ITCZ north of the equator and in the southwest corner of the model domain (Fig. 2b). Precipitation also occurred in central and tropical South America, the Gulf of Mexico, and the Caribbean Sea. The model simulated the spatial distribution of precipitation reasonably well although again there are biases in the simulations that depend on which CP scheme was employed (Fig. 4). Overall the TDK scheme simulated the spatial distribution of precipitation better than any other CP scheme, except for a positive bias in the ITCZ (Fig. 4a). The BMJ scheme also simulated the precipitation distribution reasonably well except for an overall overestimation, in particular over the Caribbean Sea and North Atlantic (Fig. 4c). Both the KFETA and SAS schemes overestimated precipitation over the Caribbean Sea and North Atlantic as well as over tropical/subtropical South America while underestimated precipitation in the ITCZ west of 110°W over the eastern Pacific (Figs. 4b,d).

b. *Monthly averaged cloud features*

Figure 5 shows the monthly mean cloud properties, including total cloud fraction, LWP, and cloud-base and

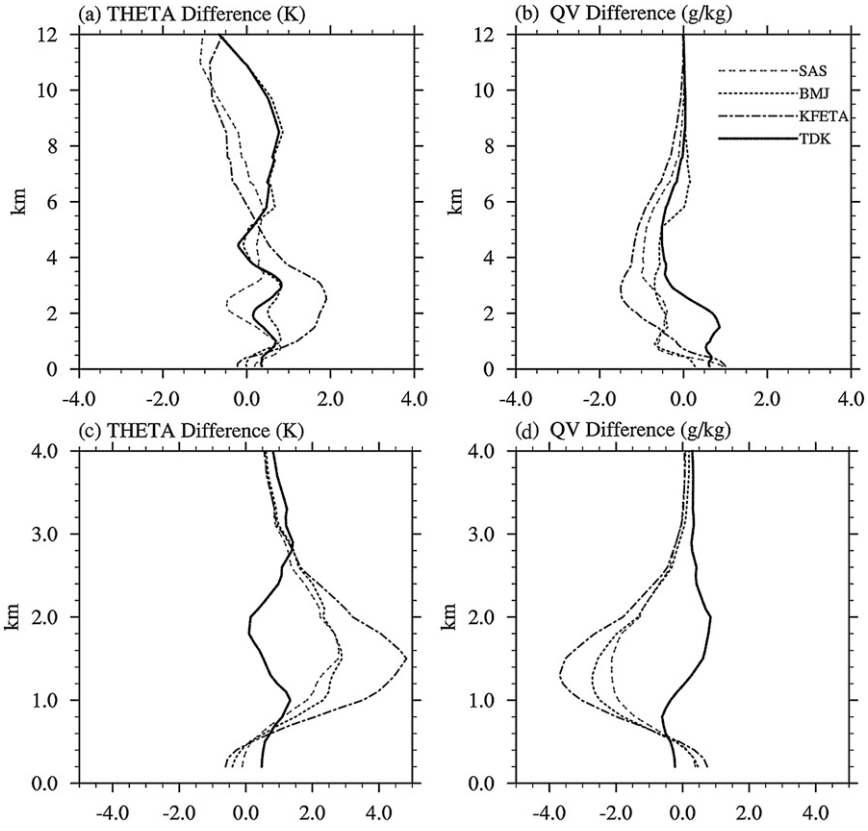

FIG. 3. Vertical profiles of the monthly mean area-averaged biases in (a),(c) potential temperature (K) and (b),(d) water vapor mixing ratio (g kg^{-1}) in the (a),(b) ITCZ region and (c),(d) the SEP region simulated with different CP schemes.

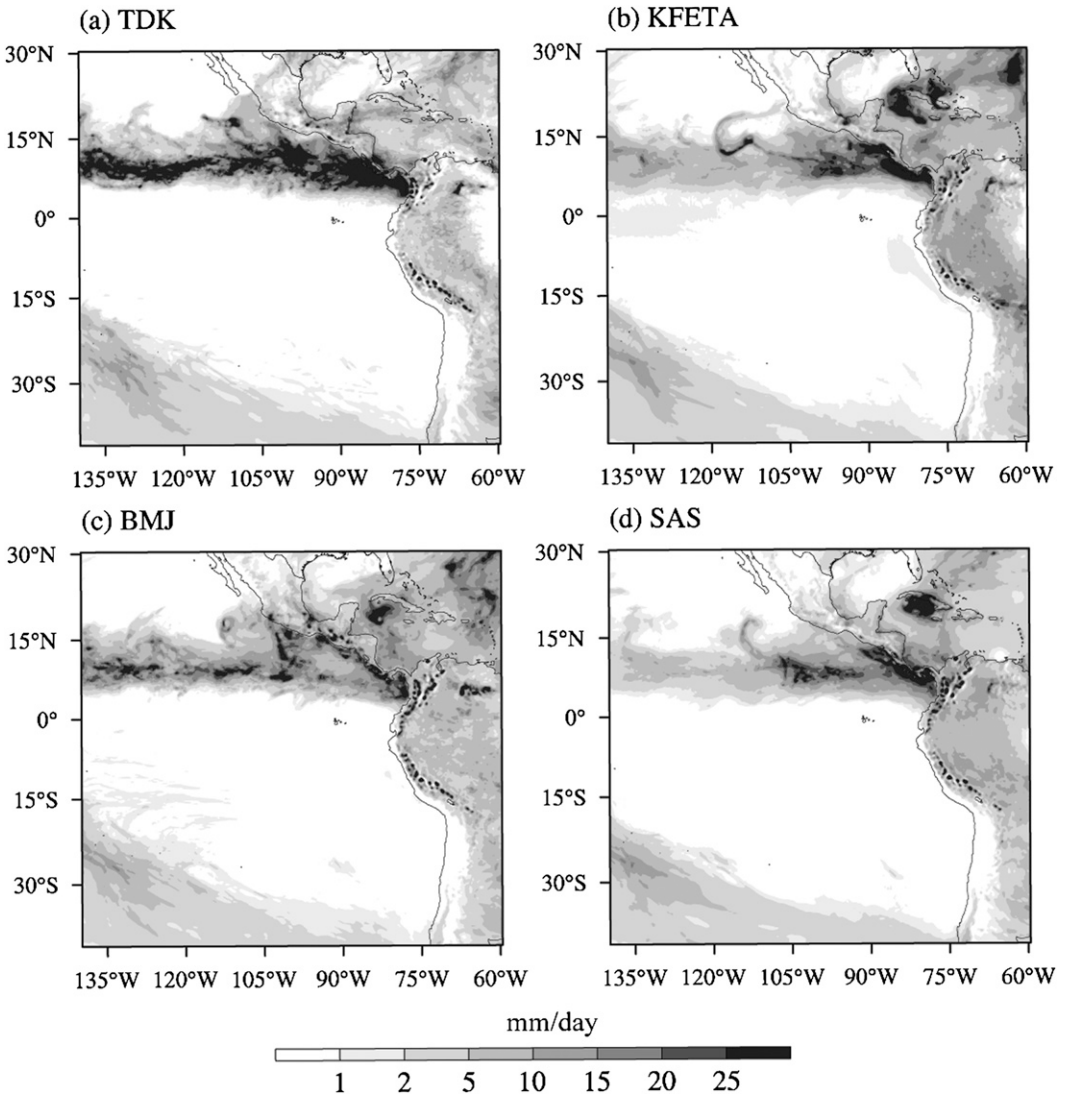

FIG. 4. Monthly mean precipitation rate (mm day^{-1}) in October 2006 in the simulations with different CP schemes: (a) TDK, (b) KFETA, (c) BMJ, and (d) SAS.

cloud-top heights from various satellite observations. The MODIS total cloud fraction shows a zonally elongated high cloud fraction north of the equator in the ITCZ region and in the southwest portion of the model domain (Fig. 5a); both were associated with precipitation (Fig. 2b). Extensive clouds also occurred over the SEP off the west coast of South America (Fig. 5a), where no significant precipitation occurred, indicating the presence of the persistent stratocumulus deck (McCaa and Bretherton 2004; Wang et al. 2004a,b). The cloud fraction decreases westward off the coast in concert with increasing SST there. The monthly mean LWP shows a spatial distribution similar to the total cloud fraction (Fig. 5b). The LWP in the ITCZ north of the equator and the Southern Hemispheric midlatitude is much larger than that in the stratocumulus region over the SEP, indicating deep liquid clouds associated with precipitation, in sharp contrast to the relatively thin nonprecipitating MBL clouds over the subtropical SEP. The monthly mean cloud-base and cloud-top heights over the SEP show a general increase westward from the coast (Figs. 5c,d). For example, the cloud base north of 30°S increases westward from lower than 0.6 km near the Peruvian coast to higher than 0.8 km to the west of 105°W. The cloud base south of 30°S is between 0.8 and 1 km. Accordingly, the cloud top north of 30°S increases from below 1.0 km near the Peruvian coast to higher than 1.6 km to the west of 105°W and that south of 30°S is generally higher than 1.4 km (Fig. 5d).

The model-simulated monthly mean total cloud fractions in October 2006 using different CP schemes are

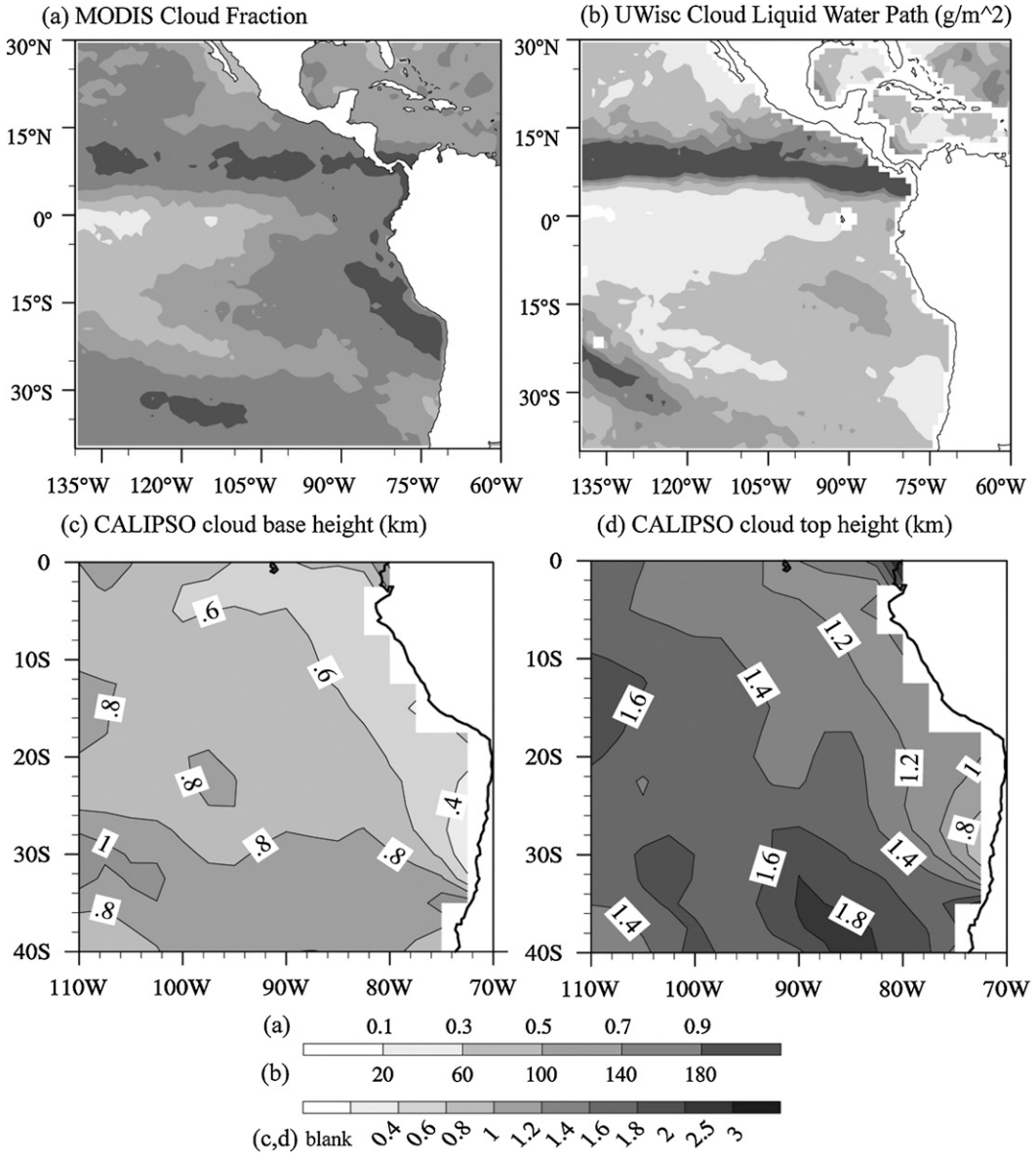

FIG. 5. The monthly mean observations in October 2006: (a) MODIS total cloud fraction, (b) UWisc cloud liquid water path (g m^{-2}), (c) the CALIPSO cloud-base height (km), and (d) the CALIPSO cloud-top height (km).

shown in Fig. 6. The model with the TDK scheme simulated the spatial distribution of total cloud fraction (Fig. 6a) very similar to the MODIS observation in both the ITCZ and SEP regions (Fig. 5a) except for an underestimation of the westward extension of low clouds west of 100°W in the subtropical SEP. The model with the KFETA scheme simulated too high cloud fractions along the Peruvian coast, but very little cloud fraction offshore to the west in the subtropical SEP. It also produced a cloud band near the equator with little precipitation south of the ITCZ (Fig. 4b), which did not appear in the MODIS cloud product (Fig. 5a). The KFETA scheme also underestimated cloud fraction in the western part of the ITCZ (Fig. 6b), consistent with the underestimation of precipitation in the same region with this scheme. The BMJ scheme simulated the spatial distribution of total cloud fraction reasonably well except for an unrealistic cloud band over and near the equator (Fig. 6c), similar to that which appeared in the simulation with the KFETA scheme. The model with the SAS scheme simulated a spatial distribution of total cloud fraction (Fig. 6d) that deviates greatly from the MODIS observation. Notably, it considerably underestimated cloud fraction in the region off the west coast of South America and in the

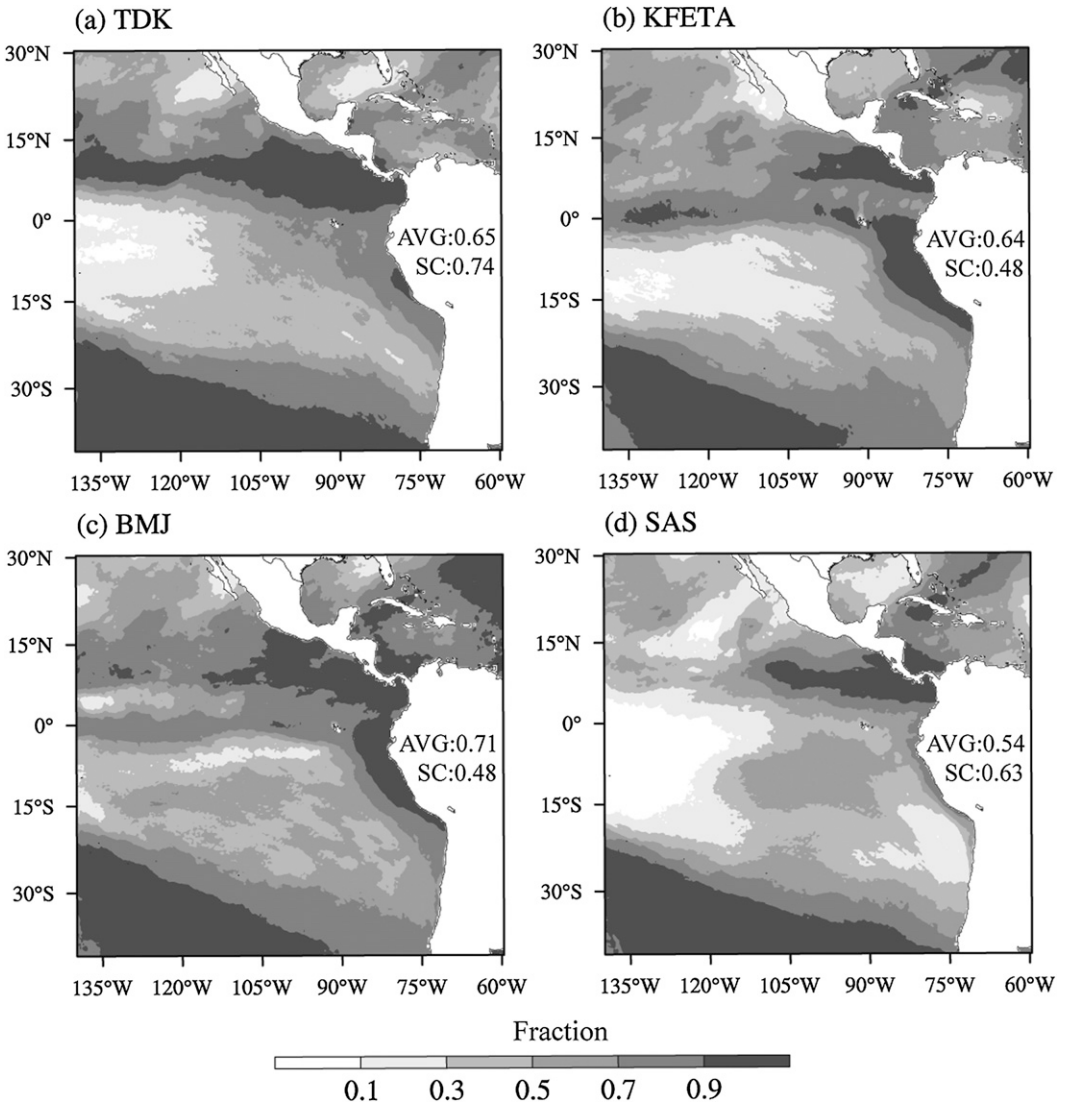

FIG. 6. The model-simulated monthly mean (October 2006) total cloud fraction from different CP schemes: (a) TDK, (b) KFETA, (c) BMJ, and (d) SAS. AVG means averaged total cloud fraction over the ocean. SC means the spatial correlation between MODIS-derived total cloud fraction (Fig. 5a) and model-simulated total cloud fraction over the ocean in the corresponding runs.

western part of the ITCZ north of the equator and over the Northern Hemisphere subtropical ocean. The former again is presumably related to the underestimated precipitation in the western part of the ITCZ (Fig. 4d). The averaged total cloud fraction (AVG) by MODIS observation over the ocean is 0.70. That for the BMJ scheme is 0.71, very close to MODIS observation. However, The BMJ scheme has the lowest spatial correlation (SC) of 0.48 with the MODIS observation. The AVG for the TDK scheme is 0.65, and the SC is 0.74, which is the highest value compared to other CP schemes (Fig. 6).

Figure 7 shows the simulated monthly mean LWP for each of the model simulations with different CP schemes (cf. with observations in Fig. 5b). The simulation with the TDK scheme (Fig. 7a) reproduces reasonably well the spatial distribution in LWP except for a slightly underestimate in the subtropical SEP (Figs. 5b and 7a). Although the model with the BMJ scheme (Fig. 7c) simulated the overall geographical distribution in LWP reasonably well, it underestimated LWP both in the ITCZ and over the subtropical SEP and simulated an unrealistic band of enhanced LWP over and near the equator in the same place as the equatorial cloud band already seen in the total cloud fraction (Fig. 6c). The simulations with both the KFETA and the SAS schemes significantly underestimated LWP over the whole model domain and

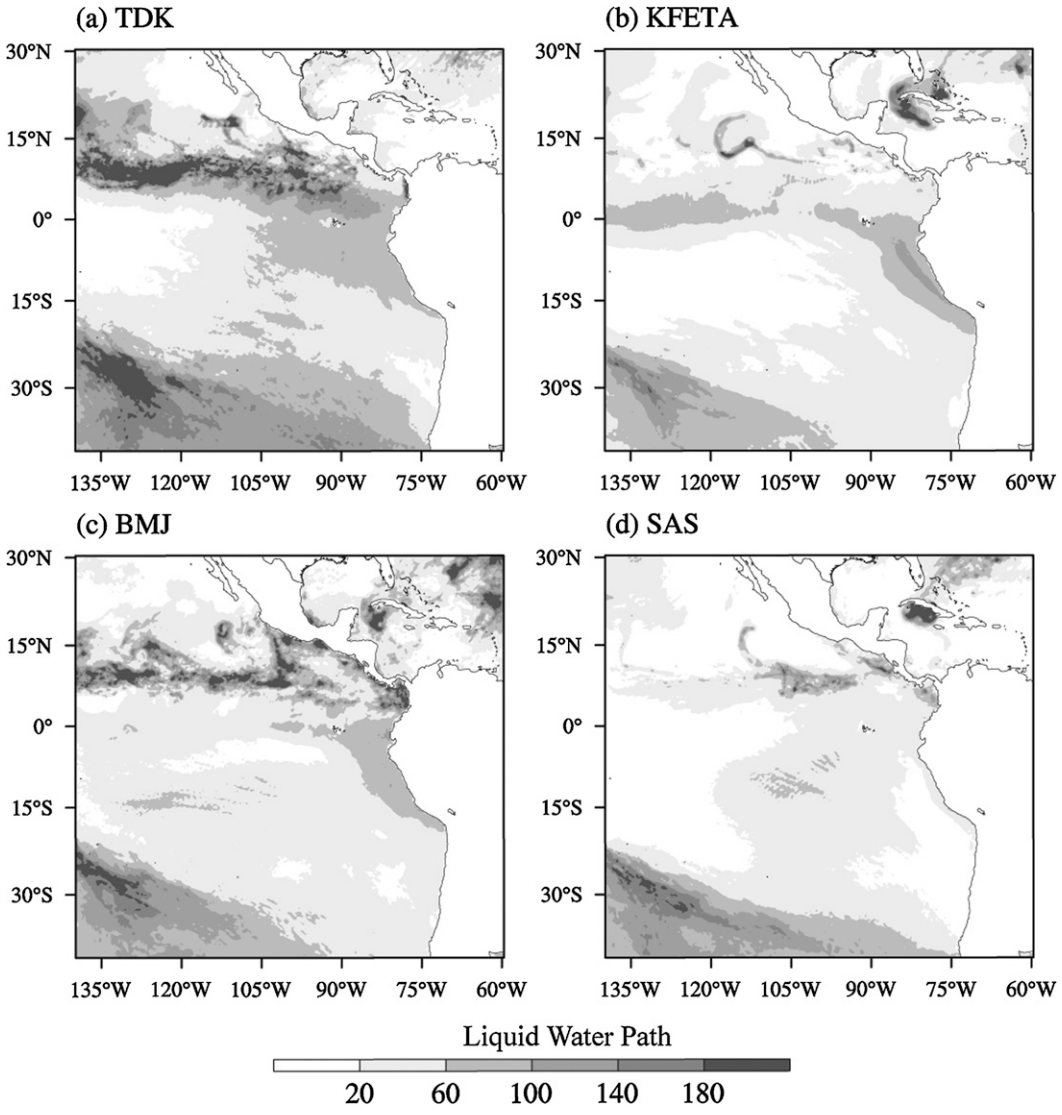

FIG. 7. The model-simulated monthly mean (October 2006) liquid water path (g m^{-2}) from different CP schemes: (a) TDK, (b) KFETA, (c) BMJ, and (d) SAS.

showed considerable bias in spatial distribution as well (Figs. 7b,d). It is apparent that the model with the TDK scheme does a more realistic job at simulating both cloud fraction and LWP than with the other three CP schemes tested here.

Figure 8 shows the monthly mean cloud-base and cloud-top heights in simulations using different CP schemes. Here for these model results we defined the model cloud-base height as the lowest level between surface and 3 km above which the daily mean cloud liquid water content exceeds 0.025 g m^{-3} and the model cloud-top height as the level below which the daily mean cloud liquid water content falls below this threshold value (Wang et al. 2011). The cloud-base–top heights simulated with the KFETA and BMJ schemes are very similar. Both the cloud top and cloud base were too low (Figs. 8b,c,f,g) compared with the CALIPSO observation (Figs. 5c,d). The TDK and SAS schemes simulated both the cloud-base and cloud-top heights reasonably well (Figs. 8a,d,e,h). The TDK scheme simulated both cloud-base and cloud-top heights about 200 m too high compared with the CALIPSO observation. Considering the fact that the CALIPSO cloud base might be a little bit too low compared to reality (see section 2c), the SAS scheme might slightly underestimate both the cloud-base and cloud-top heights near the coastal region off South America (Fig. 8d). Keeping in mind the uncertainties in the satellite retrieved cloud-base–top heights, we judge

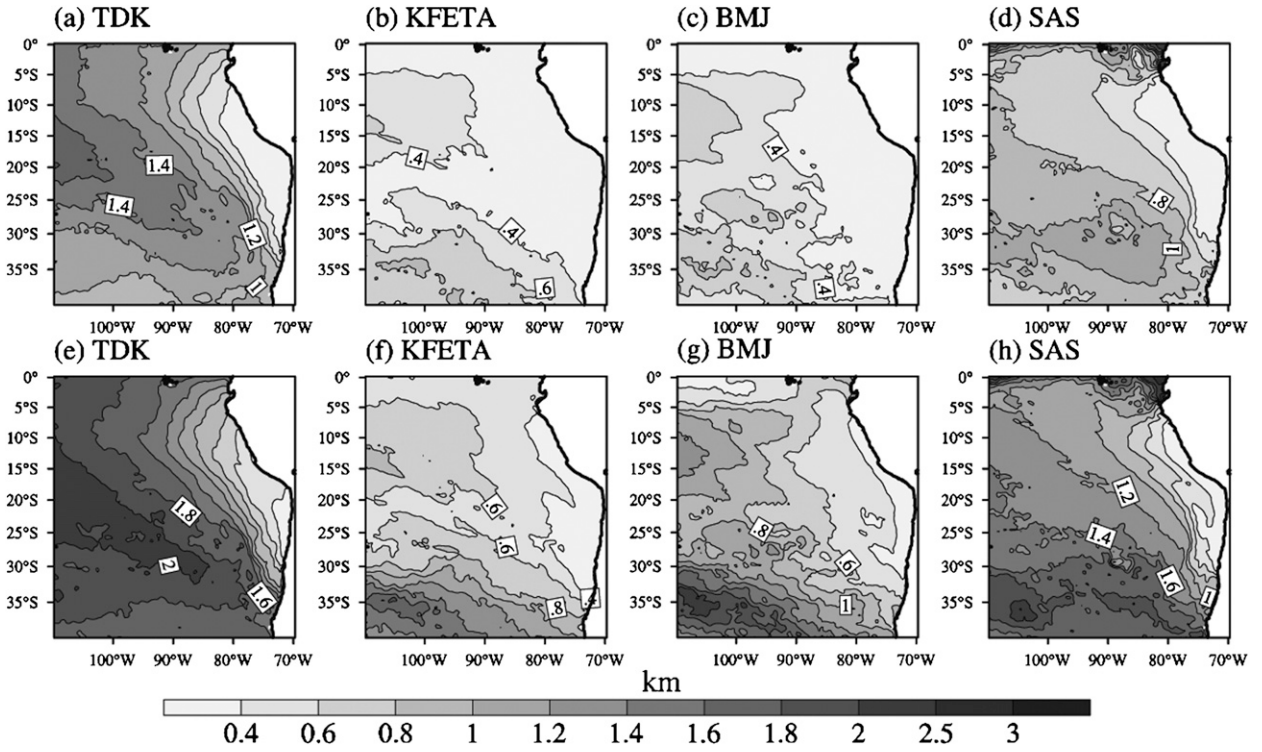

FIG. 8. The model-simulated monthly mean (October 2006) (top) cloud base and (bottom) cloud top (km) using different CP schemes: (a),(e) TDK; (b),(f) KFETA; (c),(g) BMJ; and (d),(h) SAS.

that the TDK scheme performed better than the other CP schemes tested in simulating the vertical structure of the MBL and low clouds over the SEP (see further discussion in section 3c).

c. 5-day average over the SEP

The NOAA ship cruise to the stratus buoy started on 9 October 2006 and ended on 27 October. The ship stayed near the buoy location (20°S, 85°W) for about 5 days (16–20 October). During these 5 days 29 radiosondes were launched at 3–5-h intervals and many other data were collected in this area as well (Wolfe et al. 2006). We averaged the 29 observed soundings (OBS) to construct the water vapor mixing ratio and potential temperature profiles shown in Figs. 9a,b. These are compared with an average of 40 three-hourly snapshots from the same 5 days of the model simulations. The model profiles were averaged in a $3° \times 3°$ box centered at 20°S, 85°W in order to account for any possible horizontal drift during the radiosonde ascents. The observed profiles show a typical decoupled MBL structure as observed during the 2004 stratus cruise in this region by Serpetzoglou et al. (2008). The NCEP FNL analysis captured the overall vertical structure although it did not reproduce the decoupling in moisture field at least in part because of the low vertical resolution. Among the model results with the four CP schemes, only the version employing the TDK scheme captured the basic decoupled structure of the MBL and the inversion near 1.5 km. The model versions with the other three CP schemes simulated a MBL below about 1 km, too low compared with in situ observations. They also produced a wetter near-surface layer (Fig. 9a), indicating insufficient upward moisture transport by shallow convection or PBL schemes.

Figure 10 shows the 5-day mean zonal (along 20°S) cross sections of cloud liquid water mixing ratio (shaded) and virtual potential temperature (θ_v, contours) together with the $d\theta_v/dp = 8$ K (100 hPa)$^{-1}$ contour (thick solid curves), which is a weak criterion for the presence of a temperature inversion layer (Wang et al. 2004a). Consistent with the discussion in section 3b, both KFETA and BMJ schemes produced a very low cloud layer not only near the coast but also to the west in the model domain where SST was relatively high (Figs. 10b,c). The TDK scheme simulated the westward increase in cloud layer (Fig. 10a) while the SAS scheme simulated a relative thick cloud layer with nearly constant cloud-base and cloud-top heights west of 80°W (Fig. 10d). The cloud layer simulated with the TDK scheme increased in height in response to the westward SST increase. The height of

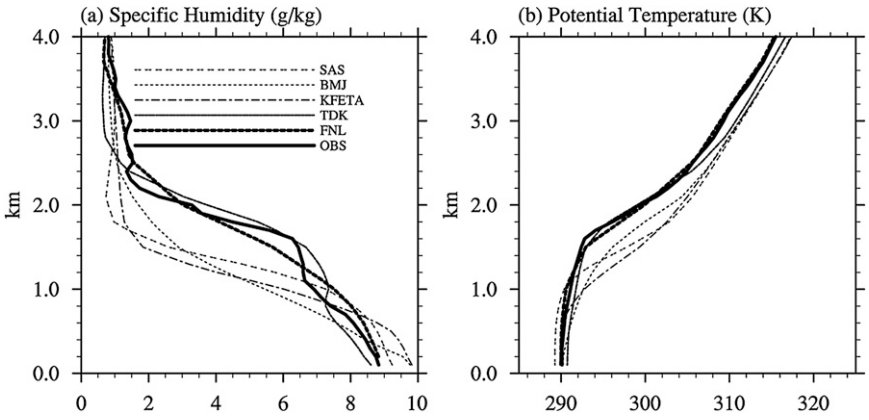

FIG. 9. The model-simulated 5-day-averaged (16–20 Oct 2006) vertical profiles of (a) water vapor mixing ratio (g kg^{-1}) and (b) potential temperature (K) at stratus buoy (20°S, 85°W) with the TDK, KFETA, BMJ, and SAS CP schemes. The corresponding profiles from in situ observation and from the FNL analysis are also given.

the simulated low cloud layer appears to be largely controlled by the location of the inversion base. As we can see from Fig. 10, the model-simulated inversion base depends on which CP scheme is employed. The TDK scheme showed the highest inversion base (Fig. 10a) while the KFETA scheme produced the lowest inversion base (Fig. 10b) among the four CP schemes, consistent with the height of the cloud layer in respective simulations. Both BMJ and SAS schemes simulated an inversion base lower than that observed, as inferred from the potential temperature profile near the stratus buoy shown in Fig. 9b.

To understand the dependence of the simulated boundary layer depth with CP schemes used, we examined the vertical profiles of potential temperature and water vapor mixing ratio tendencies due to the CP and the PBL schemes, respectively. The result in each simulation is averaged in the same 3° by 3° box near the stratus buoy (Fig. 11). Since there was no convective precipitation near the location of buoy during the simulation period (Fig. 2b), the tendency computed from the CP scheme was mainly a result of the parameterized shallow convection. Among the four CP schemes, the TDK scheme showed the most active shallow convection, which warmed the cloud layer and cooled and moistened the cloud top as a result of the evaporation of cloud water detrained from the shallow convection (Figs. 11a,b). This vertical distribution of convective heating destabilized the cloud layer and lifted the inversion base, which in turn was limited by the large-scale subsidence (Tiedtke 1989; Wang et al. 2004a). The TDK scheme also substantially dried the subcloud layer (Fig. 11b), enhancing surface latent heat flux as we can see from the tendency in water vapor mixing ratio due to the PBL scheme (Fig. 11d) and supplying more moisture to the cloud layer. The PBL tendency was nearly balanced by the tendency due to shallow convection.

Shallow convection in other CP schemes seemed to be weaker than that in the TDK scheme, a major reason why the inversion layer was lower in simulations with the KFETA, BMJ, and SAS schemes than in the simulation with the TDK scheme. Convective parameterization by the KFETA scheme produced a warming effect below about 1 km (Fig. 11a) and a drying effect below about 0.75 km and a moistening effect immediately above (Fig. 11b). The KFETA scheme was the only scheme that did not produce any convective cooling effect above the inversion base, indicating little penetrative effect due to shallow convection in that scheme. As a result, the inversion base and the inversion layer simulated with the KFETA scheme were the lowest among the four simulations (Figs. 9a,b). The low inversion layer simulated in the model with the KFETA scheme prevented the development of turbulence and vertical transport of moisture in the subcloud layer, leading to the wettest near-surface layer of any of the simulations (Fig. 9a).

The BMJ scheme simulated diffused vertical profiles in both potential temperature and water vapor mixing ratio (Fig. 9a,b). This scheme warmed the layer below about 1.5 km and substantially cooled the layer above (Fig. 11a), resulting in a relatively higher inversion layer than both the KFETA and SAS schemes (Figs. 9 and 10). Compared with other CP schemes, the BMJ scheme seemed to misrepresent the convective effect on moisture transport (Fig. 11b). It dried a very shallow layer immediately above the surface while it slightly moistened a relatively deep layer between 0.5 and 2.4 km, leading to

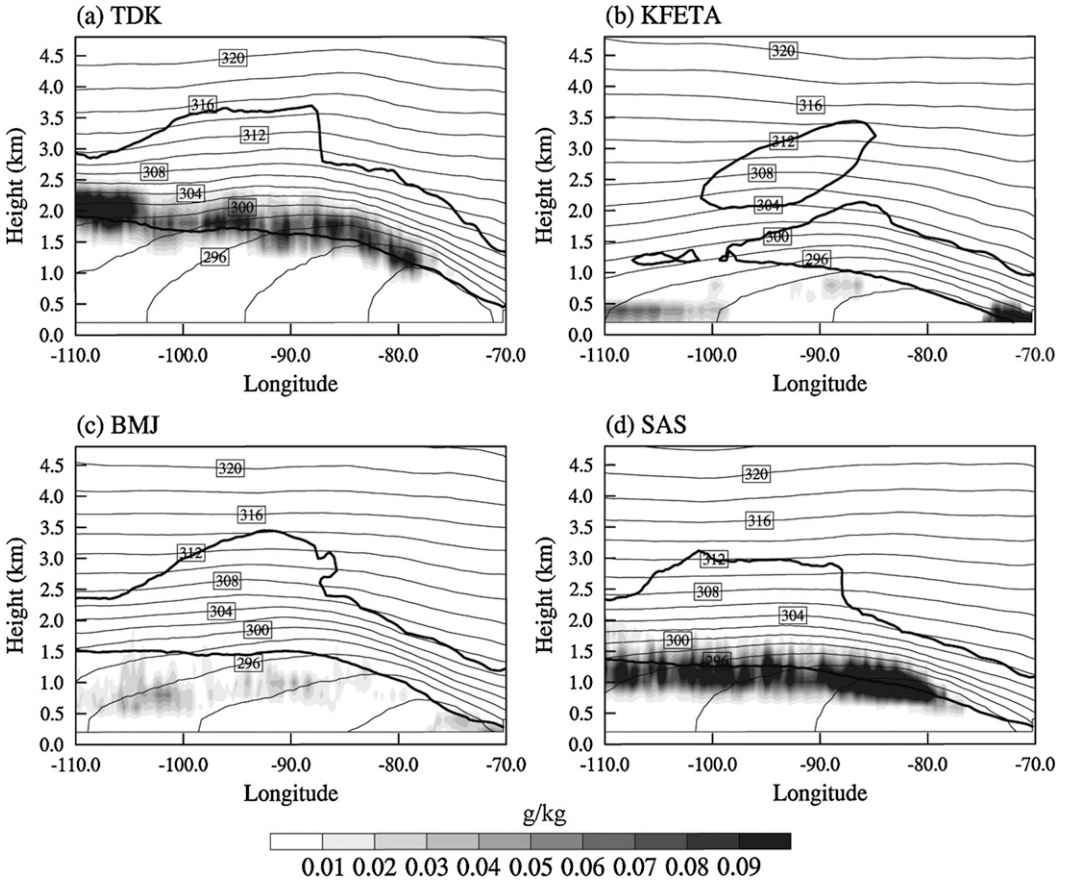

FIG. 10. The model-simulated 5-day-averaged (16–20 Oct 2006) cross sections of cloud liquid water mixing ratio (shaded, kg kg^{-1}) and virtual potential temperature (contours, K) together with the $d\theta_v/dp = 8$ K (100 hPa)$^{-1}$ contour (thick solid curves) along 20°S with different CP schemes: (a) TDK, (b) KFETA, (c) BMJ, and (d) SAS.

the smallest moistening tendency in the boundary layer due to PBL process among the 4 CP schemes (Fig. 11d). It seems that underestimation of boundary layer clouds simulated with the BMJ scheme could be partially due to the improper treatment of moisture transport due to shallow convection.

The SAS scheme simulated a boundary layer depth near the stratus buoy shallower than both the TDK scheme and observation while deeper than either the KFETA scheme or the BMJ scheme (Figs. 9a,b). Similar to the TDK scheme, the SAS scheme produced a warming and drying effect below 1.0 km and a cooling and moistening effect above. The warming rate however was much smaller than that in the TDK scheme, leading to an inversion base and a cloud layer lower than that in the simulation using the TDK scheme. The SAS scheme parameterizes the shallow convection with a simple vertical diffusion algorithm with a fixed profile of vertical diffusion coefficient (Tiedtke 1983; see appendix A). It is thus not surprising that the PBL scheme produced a quite similar vertical distribution of potential temperature and water vapor mixing ratio tendencies except for large surface heat and moisture fluxes over the ocean (Figs. 11c,d). Note that because of the upward shift in the maximum tendencies due to shallow convection relative to the PBL scheme, the height of the inversion layer was mainly maintained by the shallow convection scheme in the simulation. In addition, the strong moistening due to the parameterized PBL process in the cloud layer explains the thick and extensive boundary layer clouds in the simulation with the SAS scheme (Fig. 10d).

4. Sensitivity to PBL schemes

In the last section, we have shown that the TDK scheme newly implemented into the ARW-WRF model can better reproduce the basic MBL structure and boundary layer clouds than other CP schemes available in the current version of the model. Since in those simulations, only the YSU PBL scheme was used, the question

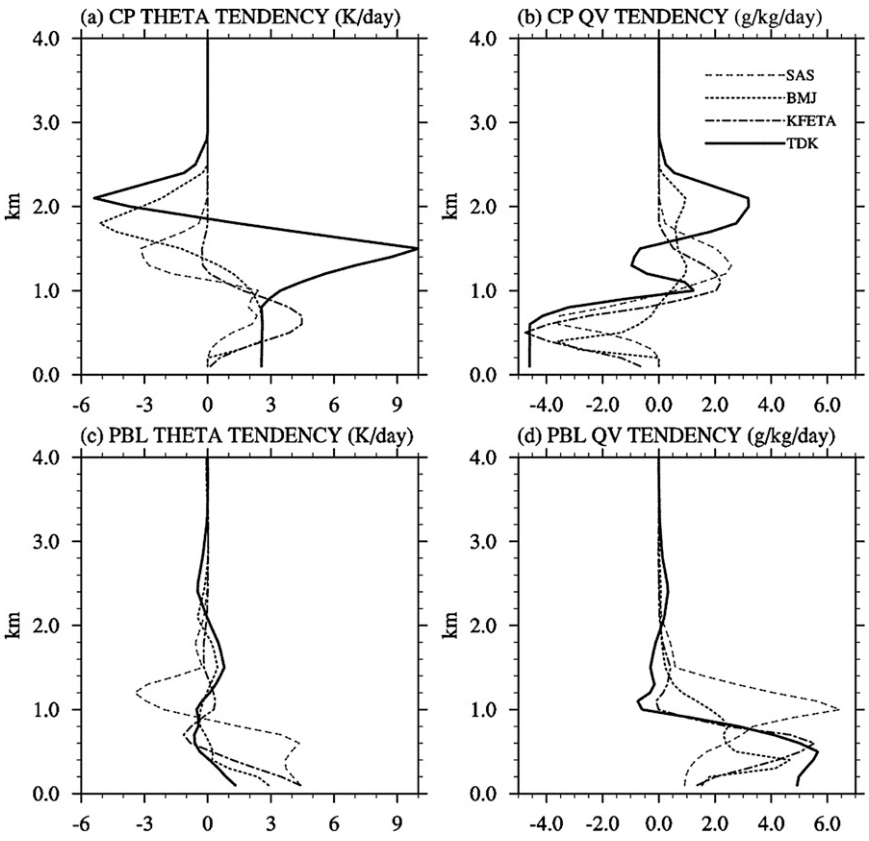

FIG. 11. The model-simulated 5-day-averaged (16–20 Oct 2006) vertical profiles of (left) potential temperature and (right) water vapor mixing ratio tendencies from (top) CP and (bottom) PBL.

arises as to how sensitive the simulation using the TDK scheme could be to the choice of the PBL scheme. In this section we will discuss results from some sensitivity experiments using different PBL schemes available in WRF model, namely the ACM2, MYJ, MYNN, and BouLac schemes (see Table 2 and appendix B).

Figure 12 shows the model-simulated monthly mean biases of MSLP and 10-m winds for the simulations with different PBL schemes. Not surprisingly, the model biases vary with the choice of PBL schemes in the simulations since the PBL schemes play a critical role in both surface fluxes and vertical mixing in the model. Overall, both the ACM2 scheme and the MYNN scheme showed somewhat smaller biases than the MYJ and BouLac schemes, as can also be seen from the RMSE listed in Table 4. The model versions employing MYJ and BouLac schemes simulated large positive bias in MSLP, in particular in the tropical/subtropical regions (Figs. 12b,d). The monthly mean biases in both potential temperature and water vapor mixing ratio in the lower troposphere averaged in the ITCZ region (Figs. 13a,b) show warm and moist biases in the simulations with ACM2 scheme, which might be related to the cold and dry bias in the FNL analysis as well. Both biases averaged in the SEP region (Figs. 13c,d) are smaller in the simulations with ACM2 and MYNN PBL schemes than in those with MYJ and BouLac PBL schemes. Nevertheless, the biases from different PBL schemes in general are still smaller than those with other CP schemes shown in Fig. 3, in particular over the SEP region. Therefore, in terms of the MBL structure over the SEP, the TDK scheme performed the best among the tested CP schemes regardless the PBL scheme used.

The use of different PBL schemes seemed not to alter significantly the spatial distribution of precipitation except in the ITCZ region (Fig. 14). Similar to the result with the YSU scheme (Fig. 4a), the model with the ACM2 scheme overestimated precipitation in the ITCZ north of the equator compared with the TRMM 3B43 products (Fig. 14a). The BouLac scheme simulated the least precipitation in the ITCZ region among the five PBL schemes (Fig. 14d). Precise comparisons with the observations are complicated by evidence that the satellite products might underestimate precipitation over the ocean (Huffman et al. 1997).

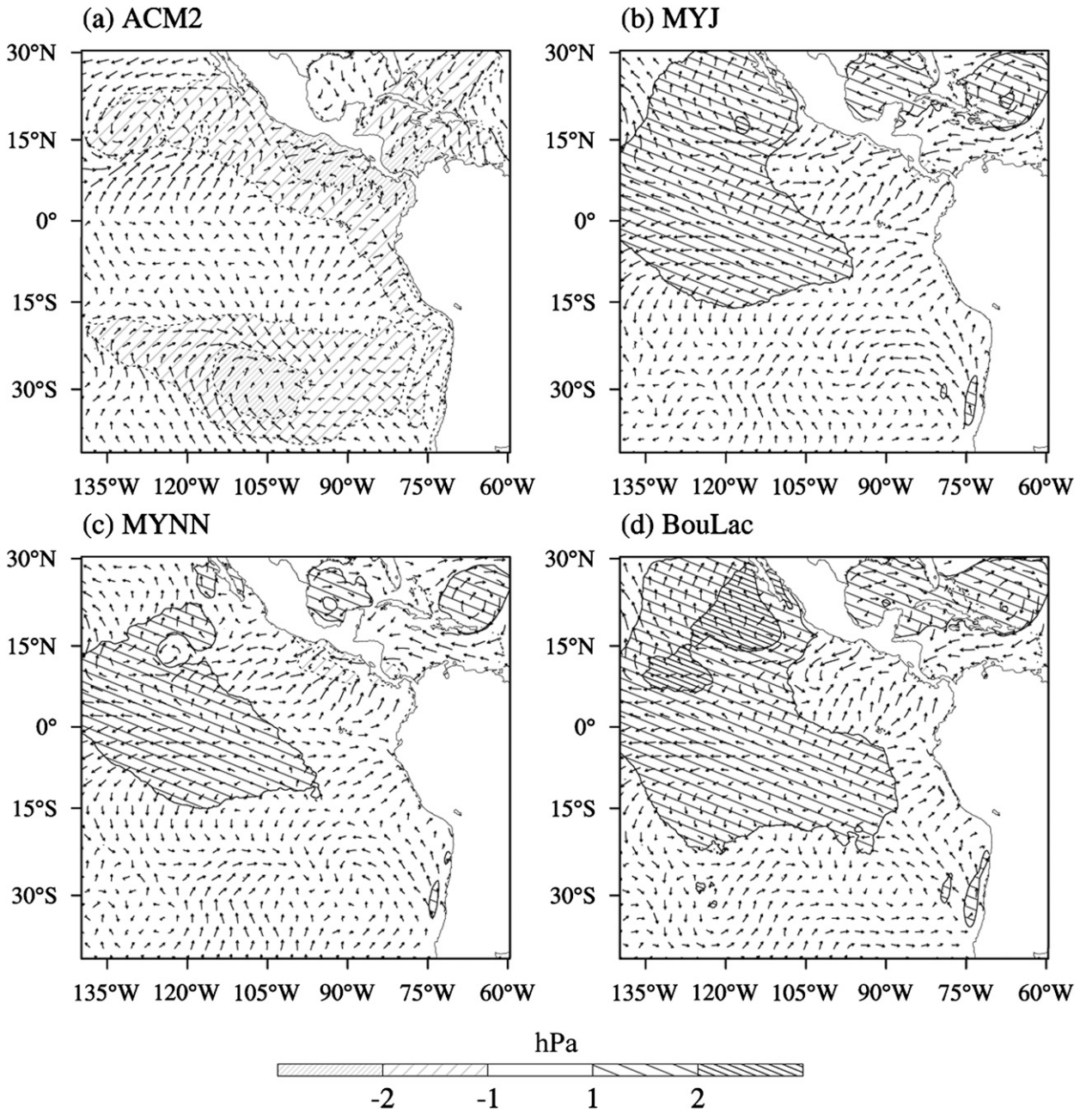

FIG. 12. Model biases in monthly mean sea level pressure (hPa, shading) and 10-m winds (m s^{-1}, vectors) from simulations using the TDK scheme with different PBL schemes: (a) ACM2, (b) MYJ, (c) MYNN, and (d) BouLac.

The simulation with each of the PBL schemes captured the overall spatial distribution of the monthly mean total cloud fraction as seen in the MODIS observations although all simulations underestimated low clouds near Chilean coast and the subtropical ocean offshore (Fig. 15). This bias is particularly apparent for the MYJ and BouLac PBL schemes. The AVG and SC for all the PBL schemes are very close. Overall, ACM2 and MYNN have higher SC, and MYJ has the lowest AVG (Fig. 15). Despite these discrepancies, the difference in performance among all PBL schemes is much smaller than that seen when the CP scheme is changed. This indicates that the improved simulation of boundary layer clouds over the SEP using TDK scheme discussed in section 3 is robust in the sense that it does not depend on the choice of a particular PBL scheme. The 5-day mean vertical profiles

TABLE 4. As in Table 3, but for using the TDK CP scheme with different PBL schemes as listed in Table 2 and described briefly in appendix B: ACM2, MYJ, MYNN, and BouLac.

	ACM2	MYJ	MYNN	BouLac
MSLP (hPa)	1.06	0.88	0.75	1.04
10-m wind speed (m s^{-1})	0.80	0.85	0.86	0.82
500-hPa height (m)	8.47	12.50	10.74	11.87

of the simulated potential temperature and water vapor mixing ratio near 20°S, 85°W did not vary significantly with different PBL schemes employed (Fig. 16). Although all the PBL schemes reproduced the decoupled MBL structure reasonably well, the subcloud layer was too dry (Fig. 16a) and the top of the inversion layer was too warm (Fig. 16b) in simulations with the MYNN, BouLac, and MYJ schemes (Fig. 16a). Nevertheless, the simulated MBL height and the cloud-base and cloud-top heights are similar in the four simulations and very close to those obtained using the YSU scheme (Fig. 9) and to the radiosonde observations.

5. Summary

In this paper, we have documented the implementation of a modified Tiedtke cumulus parameterization scheme into the latest version of the ARW-WRF model and evaluated its performance in simulating the MBL structure and low clouds over the SEP. A series of numerical experiments were conducted to compare different CP schemes and to examine the sensitivity of the simulation to the choice of different PBL schemes available in the ARW-WRF model. The simulation period corresponded with that employed in the PreVOCA model intercomparison project (Wyant et al. 2010), namely a whole month simulation for October 2006.

The model was able to simulate the large-scale atmospheric circulation in the eastern Pacific reasonably well with any of the CP schemes tested but the simulation with the newly implemented Tiedtke scheme had the smallest biases and that with the KFETA scheme showed the largest biases in both the ITCZ and SEP regions. The model with the TDK scheme simulated the wettest lower troposphere in the ITCZ region and the

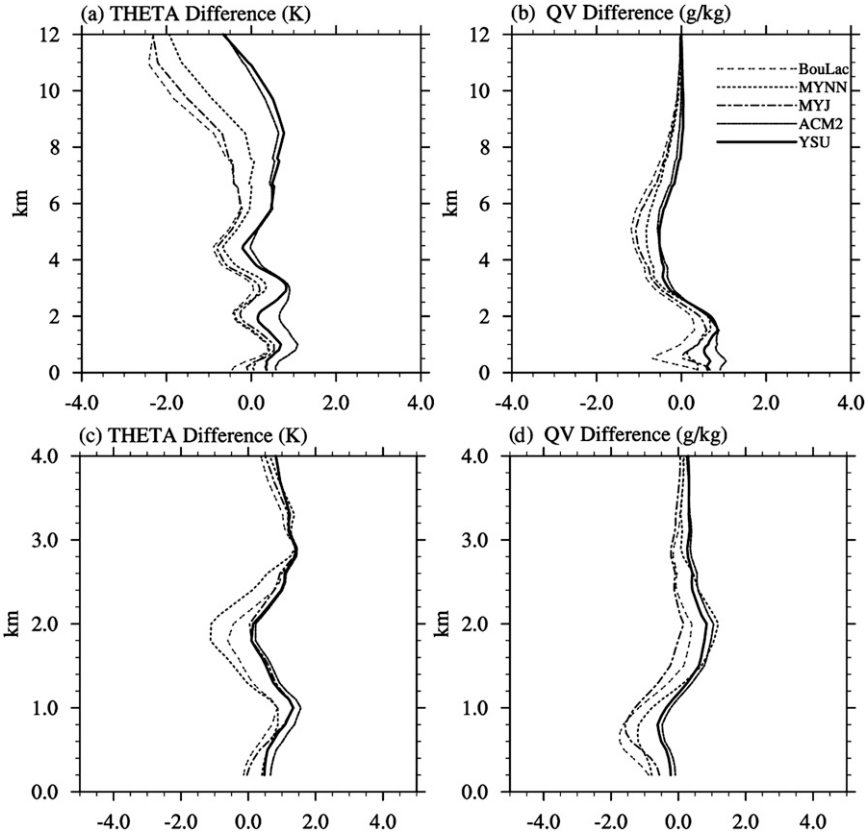

FIG. 13. Vertical profiles of the monthly mean area-averaged biases in (a),(c) potential temperature (K) and (b),(d) water vapor mixing ratio (g kg^{-1}) in the (a),(b) ITCZ region and the (c),(d) SEP region simulated using the TDK CP scheme with different PBL schemes.

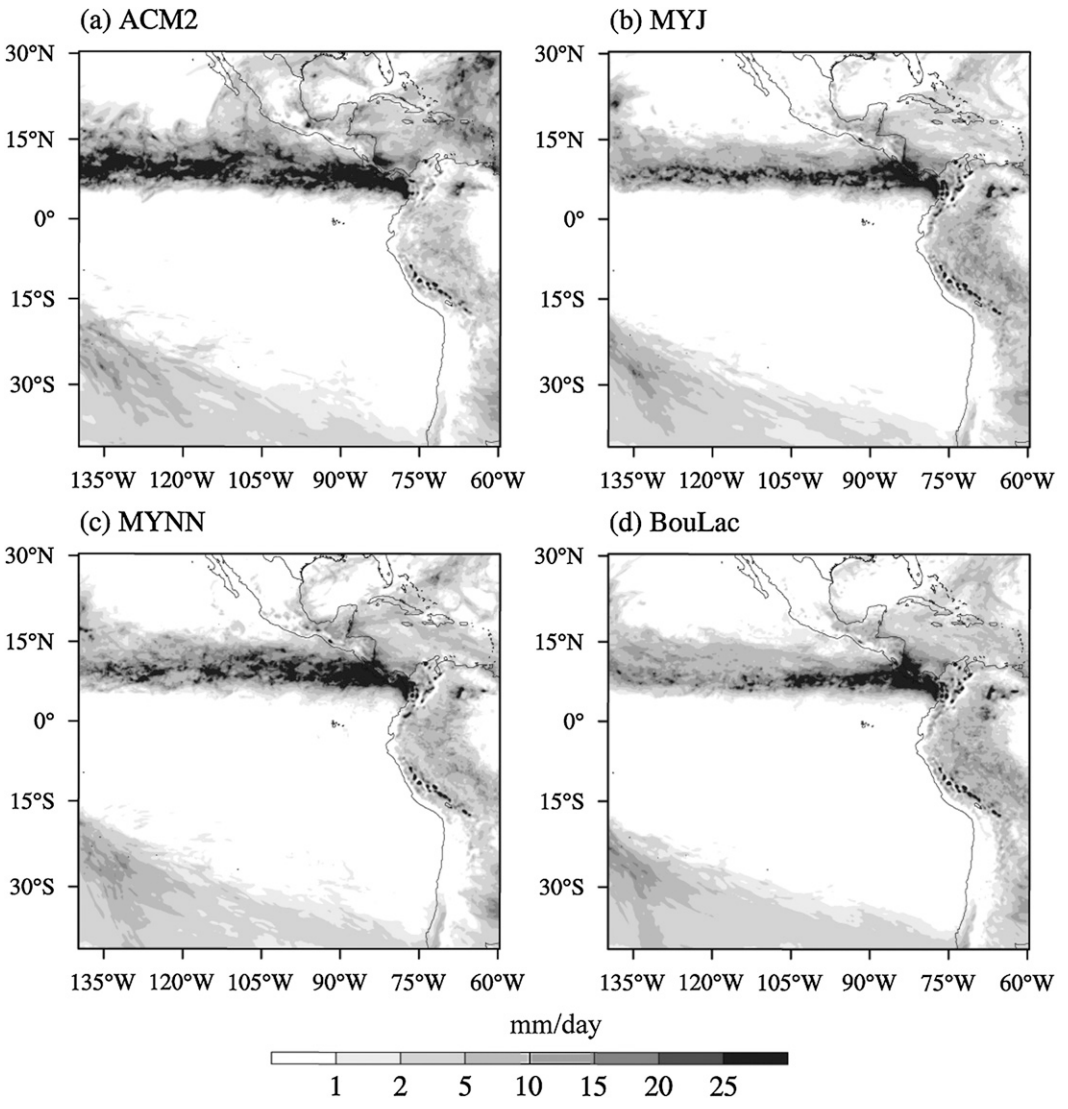

FIG. 14. Monthly mean precipitation rate (mm day^{-1}) in October 2006 in the simulations using the TDK CP scheme with different PBL schemes: (a) ACM2, (b) MYJ, (c) MYNN, and (d) BouLac.

driest near-surface layer in the SEP and was closest to observations in these aspects. Other CP schemes showed a dry bias through the depth of the free troposphere in the ITCZ and warm and dry biases in the mid–lower troposphere over the SEP. In contrast to the simulated large-scale circulation, the model-simulated boundary layer clouds were strongly dependent on the CP scheme employed. Among the four CP schemes tested, only the simulation with the TDK scheme reproduced the main features of boundary layer clouds over the eastern Pacific, including the spatial distribution, cloud LWP, and cloud-base and cloud-top heights. Use of the KFETA scheme led to a substantially underpredicted cloud fraction in the ITCZ north of the equator and simulation of a spurious cloud band near the equator. The model with the BMJ scheme also simulated the unrealistic cloud band along the equator. The model with SAS scheme underpredicted the total cloud fraction in the western part of the ITCZ and the low clouds off the west coast of South America. Use of the KFETA, BMJ, and SAS schemes all led to substantially underpredicted LWP throughout most of the model domain as well as a too shallow MBL and a too low cloud layer in the subtropical SEP.

A comparison between model simulation and observation for a 5-day mean MBL structure and low clouds near the stratus buoy (20°S, 80°W) showed that only the TDK scheme simulated reasonably well the decoupled boundary layer structure. The model versions employing the other three CP schemes all failed to reproduce the

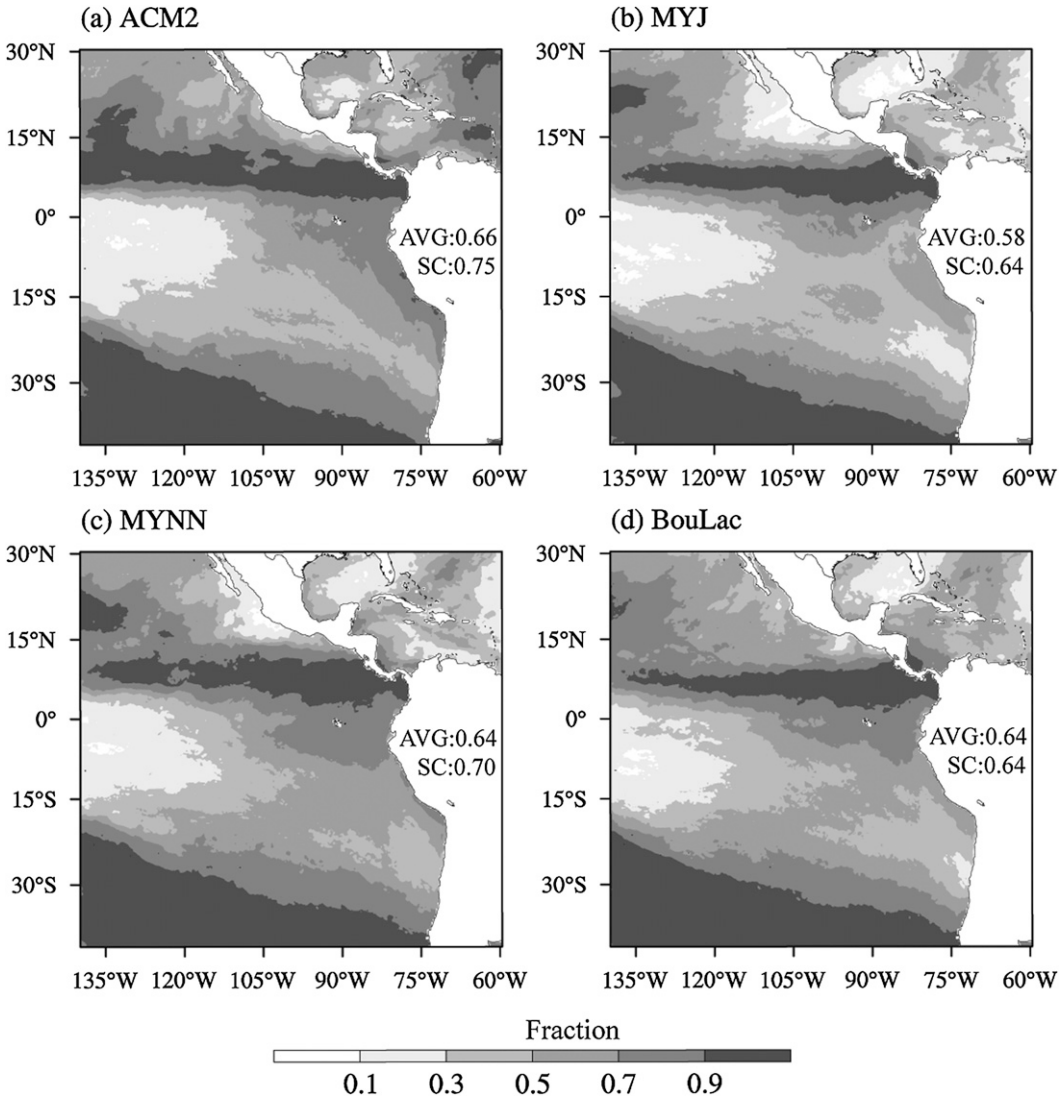

FIG. 15. The model-simulated monthly mean (October 2006) total cloud fraction using the TDK CP scheme with different PBL schemes: (a) ACM2, (b) MYJ, (c) MYNN, and (d) BouLac. AVG means averaged total cloud fraction over the ocean. SC means the spatial correlation between MODIS-derived total cloud fraction (Fig. 5a) and model-simulated total cloud fraction over the ocean in the corresponding runs.

decoupled MBL structure and simulated a well-mixed boundary layer that is too wet and too shallow, with the KFETA and BMJ schemes producing the worst results in this regard. Among the four CP schemes tested, the TDK scheme showed the most active shallow convection, which dried the subcloud layer and warmed the cloud layer, and cooled and moistened the layer immediately above the cloud top due to evaporation of cloud water detrained out of the cloud top. This substantially destabilized the cloud layer and lifted the inversion base, which in turn was stabilized by the large-scale subsidence. The drying effect in the subcloud layer from the TDK scheme also considerably enhanced the surface latent heat flux to supply moisture to the cloud layer. Shallow convection in other CP schemes seemed to be less active than that in the TDK scheme. This might be a major reason why the inversion base was too low in the simulations with those schemes. The results thus demonstrate that shallow convective parameterization is critical to the realistic simulation of MBL clouds over the eastern subtropical ocean.

To check the robustness of the TDK scheme in reproducing the MBL structure and low clouds, four additional experiments were performed to examine the sensitivity of the simulation with the TDK to the choice of different PBL schemes. The results showed that the successful aspects of

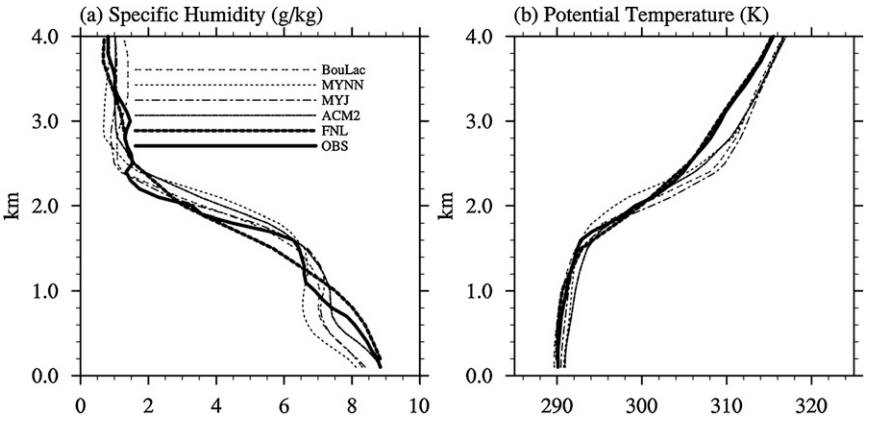

FIG. 16. The model-simulated 5-day-averaged (16–20 Oct 2006) vertical profiles of (a) water vapor mixing ratio (g kg^{-1}) and (b) potential temperature (K) at stratus buoy (20°S, 85°W) with different PBL schemes (see Table 2) and the TDK CP scheme.

the cloud simulation were not strongly dependent on the choice a particular PBL scheme. However, simulations with both the MYJ and BouLac schemes showed relatively large biases in both the large-scale circulation and boundary layer structure. The YSU and ACM2 schemes are found to be the best in these aspects, although the model employing these two schemes overpredicted the precipitation in the ITCZ region.

We note that while the TDK CP scheme performed better than other CP schemes in simulating the MBL structure and low clouds over the eastern Pacific, there are still considerable biases in the simulation even in the best versions (e.g., the TDK scheme with YSU or ACM2 boundary layer scheme). Notably the simulations underpredict low cloud fraction and LWP to some degree between 15°–25°S west of 95°W in the subtropical SEP. The model also simulates a cloud layer that is slightly too high west of about 90°W and it also overpredicts precipitation in the ITCZ north of the equator. To achieve further improvements it is necessary to examine the performance of the treatments of other interactive physics in the model, such as the grid-resolved cloud microphysics and the cloud–radiation interactions (e.g., Wang et al. 2004b; Lauer et al. 2009).

Acknowledgments. The authors are grateful to two anonymous reviewers for helpful comments. This research was supported by NOAA/CPPA Grant NA07OAR4310257 and DOE Regional and Global Climate Modeling (RCGM) Program Grant ER64840. Additional support was provided by the Japan Agency for Marine-Earth Science and Technology (JAMSTEC), by NASA through Grant NNX07AG53G, and by NOAA through Grant NA09OAR4320075, which sponsor research at the International Pacific Research Center.

APPENDIX A

Cumulus Parameterization Schemes

a. KFETA scheme

The KFETA (the new KF) scheme is a mass flux parameterization for cumulus convection (Kain 2004). It uses the Lagrangian parcel method (e.g., Simpson and Wiggert 1969; Kreitzberg and Perkey 1976), including vertical momentum dynamics (Donner 1993), to estimate whether instability exists, whether any existing instability will become available for cloud growth, and what the properties of any convective clouds might be.

1) THE TRIGGER FUNCTION

This is the task to find the potential source layers for convective clouds [e.g., updraft source layers (USLs)]. At first a ''parcel'' is defined beginning at the surface to find whether it is buoyant and its vertical velocity remains positive. The parcel is assigned a temperature perturbation linked to the magnitude of grid-resolved vertical motion. The specific formula for this perturbation is

$$\delta T_{\mathrm{vv}} = k[w_g - c(z)]^{1/3}, \tag{A1}$$

where k is a unit number with dimensions K s$^{1/3}$ cm$^{-1/3}$, w_g is an approximate running-mean grid-resolved vertical velocity at the LCL (cm s^{-1}), and $c(z)$ is a threshold vertical velocity. Use this perturbation term allows us to effectively eliminate most parcels as candidates for deep convection. If the resulting temperature is still less than the environmental value (i.e., $T_{\mathrm{LCL}} + \delta T_{\mathrm{vv}} < T_{\mathrm{env}}$), this parcel is eliminated from consideration, then the base of the USL is moved up one model level, and the above test

is repeated for a new potential USL. The initial vertical velocity w_{p0} for the parcel is loosely based on the parcel buoyancy equation and is given by

$$w_{p0} = 1.0 + 0.5\left[\frac{2G(Z_{LCL} - Z_{USL})\delta T_{vv}}{T_{env}}\right]^{1/2}, \qquad \text{(A2)}$$

where Z_{USL} is the height at the base of the USL, and G is the gravitational acceleration. Currently $(Z_{LCL} - Z_{USL})$ is given a constant 500 m in ARW-WRF version 3.2.1. The w_{p0} is between 1 and 3 m s^{-1}.

Above the LCL, parcel vertical velocity is estimated at each model level using the Lagrangian parcel method, including the effects of entrainment, detrainment, and water loading. Thus, the updraft model plays an important role in determining cloud depth. If vertical velocity remains positive over a depth that exceeds a specified minimum cloud depth (D_{min}), deep convection is activated using this USL. In the new KF scheme, the minimum cloud depth could be as thin as 2 km.

In the modified KF scheme, shallow convection is activated when all of the criteria for deep convection are satisfied except that the cloud model yields an updraft shallower than the minimum cloud depth. Based on Eq. (A1), if δT_{vv} is negative, δT_{vv} is set to zero. With this change, shallow convection is not suppressed by subsidence at the LCL. Without a positive perturbation, a parcel must be warmer than its environment at its LCL to satisfy the first test of the KF trigger function. This implies that the subcloud-layer lapse rate must be superadiabatic, as during strong daytime heating over land, for KF shallow convection to activate when air is sinking on resolved scales at the LCL. Shallow convection is activated only after every potential USL in the lowest 300 hPa has been rejected as a candidate for deep convection. If deep convection fails to activate, but one or more shallow clouds are found, the deepest "shallow" cloud is activated. For computational reasons, the value of cloud radius R is not changed for shallow clouds (e.g., 1000 m or a little bit more than 1000 m).

2) MASS FLUX FORMULATION

The two-way exchange of mass between clouds and their environment is modulated at each vertical level by a buoyancy sorting mechanism at the interface of clear and cloudy air. The entrainment–detrainment scheme allows vertical profiles of both updraft moisture detrainment and updraft vertical mass flux to vary in a physically realistic way as a function of the cloud-scale environment.

3) CLOSURE ASSUMPTION

The KF scheme uses a convective available potential energy (CAPE) closure. Basically, mass is rearranged in a column using the updraft, downdraft, and environmental mass fluxes until at least 90% of CAPE is removed. The CAPE was computed on the basis of undiluted parcel ascent. This approach usually decreases the CAPE significantly and, as a result, provides reasonable rainfall rates for a broad range of convective environments.

Parameterized shallow clouds are modulated by a different closure assumption. In particular, the cloud base mass flux M_{u0} is assumed to be a function of turbulent kinetic energy (TKE) in the subcloud layer:

$$M_{u0} = \begin{cases} \left(\frac{TKE_{max}}{k_0}\right)\left(\frac{m_{USL}}{\tau_C}\right) TKE_{MAX} < 10 \\ \left(\frac{10}{k_0}\right)\left(\frac{m_{USL}}{\tau_C}\right) TKE_{MAX} \geq 10 \end{cases}, \qquad \text{(A3)}$$

where τ_c is the convective time scale, ranging from 2400 s, m_{USL} is the amount of mass in the USL (kg), and $k_0 = 10$ m^2 s^{-2}. Currently, TKE_{max} is given a constant value of 5 m^2 s^{-2} in the ARW-WRF version 3.2.1.

b. *Betts–Miller–Janjić (BMJ) scheme*

The BMJ scheme is a convective adjustment scheme (Janjić 1994, 2000). The deep convection is viewed as a thermodynamically driven process that transports heat and moisture upward in order to remove or reduce the conditional instability. The deep convection profiles and relaxation time are variable and depend on the cloud efficiency, a nondimensional parameter that characterizes the convective regime (Janjić 1994).

Three conditions are required to trigger convection: some CAPE, convective cloud depth exceeding a threshold value, and moist soundings. A reference profile is a climatologically defined postconvective state, defined by points at the cloud base, cloud top, and freezing level. Different reference profiles can be constructed and employed by the scheme as needed.

The shallow cumulus scheme is also a moist adjustment scheme (Betts 1986; Betts and Miller 1986). The shallow convection is a process operating between a buoyant layer and an inversion aloft. The inversion prevents the occurrence of the penetrative convection. The moisture is transported upward and the heat is transported downward. Thus, the shallow convection maintains a delicate balance with a low entropy yield. The moisture profile is derived from the requirement that the entropy change be small and nonnegative (Janjić 1994). The computation of deep convection can change to shallow convection when the next two situations are met: negative precipitation is encountered and the negative entropy change, even if precipitation is positive.

c. Simplified Arakawa–Schubert (SAS) scheme

This is a mass flux parameterization scheme as well. Penetrative convection is parameterized following Pan and Wu (1995), which is based on Arakawa and Schubert (1974) as simplified by Grell (1993) and with a saturated downdraft. Convection occurs when the cloud work function exceeds a certain threshold. Mass flux of the cloud is determined using a quasi-equilibrium assumption based on this threshold cloud work function. The cloud work function is a function of temperature and moisture in each air column of the model grid point. The temperature and moisture profiles are adjusted toward the equilibrium cloud function within a specified time scale using the deduced mass flux. A major simplification of the original Arakawa–Shubert scheme is to consider only the deepest cloud and not the spectrum of clouds. The cloud model incorporates a downdraft mechanism as well as the evaporation of precipitation. Entrainment of the updraft and detrainment of the downdraft in the subcloud layers are included. Downdraft strength is based on the vertical wind shear through the cloud. The critical cloud work function is a function of the cloud-base vertical motion. As the large-scale rising motion becomes strong, the cloud work function (similar to CAPE) is allowed to approach zero (neutral stability). The pressure effect on the convective air parcel is parameterized in the form of entrainment.

Following Tiedtke (1983), shallow convection is parameterized as an extension of the vertical diffusion scheme. Shallow convection occurs where convective instability exists but no deep convection occurs. The cloud base is determined from the lifting condensation level and the vertical diffusion is invoked between the cloud top and the cloud base. A fixed profile of vertical diffusion coefficient is assigned for the mixing process across the cloud layer.

APPENDIX B

Planetary Boundary Layer Schemes

The YSU PBL scheme (Hong et al. 2006) is a revised version of the mediun-range forecast (MRF) scheme (Troen and Mahrt 1986; Hong and Pan 1996). The major revision is the inclusion of an explicit treatment of entrainment processes at the top of the PBL (inversion layer). In the mixed layer, the turbulence diffusion equations for prognostic variables (C, u, v, θ, q, q_c, and q_i) can be expressed by

$$\frac{\partial C}{\partial t} = \frac{\partial}{\partial z}\left[K_c\left(\frac{\partial C}{\partial z} - \gamma_c\right) - \overline{(w'c')}_h\left(\frac{z}{h}\right)^3\right], \quad \text{(B1)}$$

where K_c is the eddy diffusivity coefficient and γ_c is a correction to the local gradient due to contribution by large-scale eddies. It also includes an asymptotic entrainment flux term $\overline{(w'c')}_h(z/h)^3$ in the inversion layer. An enhanced stable boundary layer diffusion algorithm (Hong et al. 2006) is also devised that allows deeper mixing in windier conditions. The momentum diffusivity coefficient is formulated by the PBL height and velocity scale in the mixed layer. The local diffusion scheme, the so-called local K approach (Louis 1979) is utilized for free atmospheric diffusion above the mixed layer.

The MYJ (Janjić 1990, 1996, 2002) represents a nonsingular implementation of the Mellor–Yamada level 2.5 turbulence closure model (Mellor and Yamada 1982) through the full range of atmospheric turbulent regimes. The MYNN (Nakanishi and Niino 2004) is also a PBL scheme based on the Mellor–Yamada scheme, but it has both level 2.5 and level 3.0 options (in this paper, the 2.5 level scheme is used in our comparison). Both the MYJ and MYNN schemes start with the same basic form of the TKE equation. The eddy diffusivity coefficient for the MYJ and MYNN schemes is

$$K_{\text{Ø}} = S_{\text{Ø}} q l_m, \quad \text{(B2)}$$

where $q = \text{TKE}^{1/2}$, l_m is the master length scale, $S_{\text{Ø}}$ is a dimensionless stability function, and Ø can represent momentum, heat, or moisture. The first difference between the MYJ and MYNN schemes is how to define the master mixing lengths.

For the MYJ scheme, within the PBL, the master mixing length is

$$l_m = l_0 \frac{kz}{kz + l_0}, \quad \text{(B3)}$$

where

$$l_0 = 0.23 \frac{\int_0^{z_i} zq\,dz}{\int_0^{z_i} q\,dz}, \quad \text{(B4)}$$

where k is the von Kármán constant, z is the height from the surface, and z_i is the height of the mixed layer. Above the PBL, the master mixing length is

$$l_m = 0.23\Delta Z, \quad \text{(B5)}$$

where ΔZ is the thickness of the model layer in the vertical.

For the MYNN scheme, the mixing length l_m is determined by the surface layer length l_s turbulent length l_t and buoyancy length l_b namely,

$$\frac{1}{l_m} = \frac{1}{l_s} + \frac{1}{l_t} + \frac{1}{l_b}. \quad \text{(B6)}$$

The surface layer length scale l_s is a function of the dimensionless height ($\zeta = Z/L$), where L is the Monin–Obukhov length:

$$l_s = \begin{cases} kz/3.7 & \text{if} \quad \zeta > 1, \\ kz(1 + 2.7\zeta)^{-1} & \text{if} \quad 0 \geq \zeta > 1, \\ kz(1 - 100\zeta)^{0.2} & \text{if} \quad \zeta < 0. \end{cases} \quad \text{(B7)}$$

The turbulent length scale l_t is the same as l_0 in (B4), but integrated to $z = \infty$. For stable conditions, the buoyancy length scale l_b is

$$l_b = \begin{cases} q/N & \partial\theta_v/\partial z > 0 \quad \text{and} \quad \zeta \geq 0, \\ [1 + 5(q_c/l_t N)^{1/2}]q/N & \partial\theta_v/\partial z > 0 \quad \text{and} \quad \zeta \geq 0, \\ \infty & \partial\theta_v/\partial z \leq 0 \end{cases} \quad \text{(B8)}$$

where $N \equiv [(g/\theta_0)\partial\theta_v/\partial z]^{1/2}$, and $q_c \equiv [(g/\theta_0)\langle w\theta_v\rangle_g l_t]^{1/3}$.

The second difference is that the MYNN scheme uses a partial-condensation scheme following Sommeria and Deardorff (1977) and Mellor (1977) to take into account condensational processes by assuming a probability distribution of physical quantities around their ensemble averages to be a Gaussian distribution (see Nakanishi and Niino 2004). Besides those two differences, the PBL height in the MYJ scheme is determined to be where q falls below a critical value (0.001 m^2 s^{-2}), while there is no dependence on the PBL height in the MYNN scheme.

The BouLac scheme of Bougeault and Lacarrere (1989) is also a 1.5-order closure scheme. The characteristic length for turbulent eddies is recomputed by limiting it in some range. The eddy diffusivity coefficient is

$$K_{\emptyset} = 0.4 l_m q. \quad \text{(B9)}$$

In the current version the eddy diffusivity coefficient for momentum and heat has the same value (i.e., the Prandtl number is 1).

The ACM2 PBL scheme (Pleim 2007a,b) has a first-order eddy diffusion component in addition to the explicit nonlocal term. For stable or neutral conditions, the ACM2 scheme shuts off nonlocal transport and uses local closure, and it transitions smoothly from eddy diffusion in stable conditions to the combined local and nonlocal transport in unstable conditions.

REFERENCES

Arakawa, A., and W. H. Schubert, 1974: Interaction of a cumulus cloud ensemble with the large-scale environment, Part I. *J. Atmos. Sci.,* **31,** 674–701.

Awan, N. K., H. Truhetz, and A. Gobiet, 2011: Parameterization-induced error characteristics of MM5 and WRF operated in a climate mode over the Alpine region: An ensemble-based analysis. *J. Climate,* **24,** 3107–3123.

Betts, A. K., 1986: A new convective adjustment scheme. Part I: Observational and theoretical basis. *Quart. J. Roy. Meteor. Soc.,* **112,** 677–691.

——, and M. J. Miller, 1986: A new convective adjustment scheme. Part II: Single column tests using GATE wave, BOMEX, and arctic air-mass data sets. *Quart. J. Roy. Meteor. Soc.,* **112,** 693–709.

Bougeault, P., and P. Lacarrere, 1989: Parameterization of orography-induced turbulence in a mesobeta-scale model. *Mon. Wea. Rev.,* **117,** 1872–1890.

Bretherton, C. S., J. R. McCaa, and H. Grenier, 2004: A new parameterization for shallow cumulus convection and its application to marine subtropical cloud-topped boundary layers. Part I: Description and 1D results. *Mon. Wea. Rev.,* **132,** 864–882.

Brunke, M. A., S. P. de Szoeke, P. Zuidema, and X. Zeng, 2010: A comparison of ship and satellite measurements of cloud properties in the southeast Pacific stratus deck. *Atmos. Chem. Phys. Discuss.,* **10,** 3301–3318.

Bukovsky, M. S., and D. J. Karoly, 2009: Precipitation simulations using WRF as a nested regional climate model. *J. Appl. Meteor. Climatol.,* **48,** 2152–2159.

Chen, F., and J. Dudhia, 2001: Coupling an advanced land-surface/hydrology model with the Penn State/NCAR MM5 modeling system. Part I: Model description and implementation. *Mon. Wea. Rev.,* **129,** 569–585.

Collins, W. D., and Coauthors, 2004: Description of the NCAR Community Atmosphere Model (CAM3.0). NCAR Tech. Note NCAR/TN-464+STR, 226 pp.

de Szoeke, S. P., Y. Wang, S.-P. Xie, and T. Miyama, 2006: The effect of shallow convection on the eastern Pacific climate in a coupled model. *Geophys. Res. Lett.,* **33,** L17713, doi:10.1029/2006GL026715.

Donner, L. J., 1993: A cumulus parameterization including mass fluxes, vertical momentum dynamics, and mesoscale effects. *J. Atmos. Sci.,* **50,** 889–906.

Gregory, D., J.-J. Moncrette, C. Jakob, A. C. M. Beljaars, and T. Stockdale, 2000: Revision of the convection, radiation and cloud schemes in the ECMWF model. *Quart. J. Roy. Meteor. Soc.,* **126,** 2685–1710.

Grell, G. A., 1993: Prognostic evaluation of assumptions used by cumulus parameterizations. *Mon. Wea. Rev.,* **121,** 764–787.

Hannay, C., D. L. Williamson, J. J. Hack, J. T. Kiehl, J. G. Olson, S. A. Klein, C. S. Bretherton, and M. Köhler, 2009: Evaluation of forecasted southeast Pacific stratocumulus in the NCAR, GFDL, and ECMWF models. *J. Climate,* **22,** 2871–2889.

Hong, S.-Y., and H.-L. Pan, 1996: Nonlocal boundary layer vertical diffusion in a medium-range forecast model. *Mon. Wea. Rev.,* **124,** 2322–2339.

——, and J. Lim, 2006: The WRF Single-Moment 6-Class Microphysics Scheme (WSM6). *J. Korean Meteor. Soc.,* **42,** 129–151.

——, H.-M. H. Juang, and Q. Zhao, 1998: Implementation of prognostic cloud scheme for a regional spectral model. *Mon. Wea. Rev.,* **126,** 2621–2639.

——, Y. Noh, and J. Dudhia, 2006: A new vertical diffusion package with an explicit treatment of entrainment processes. *Mon. Wea. Rev.,* **134,** 2318–2341.

Huffman, G. J., and Coauthors, 1997: The Global Precipitation Climatology Project (GPCP) combined precipitation dataset. *Bull. Amer. Meteor. Soc.,* **78,** 5–20.

Janjić, Z. I., 1990: The step-mountain coordinate: Physical package. *Mon. Wea. Rev.,* **118,** 1429–1443.

——, 1994: The step-mountain eta coordinate model: Further developments of the convection, viscous sublayer, and turbulence closure schemes. *Mon. Wea. Rev.,* **122,** 927–945.

——, 1996: The surface layer in the NCEP Eta Model. Preprints, *11th Conf. on Numerical Weather Prediction*, Norfolk, VA, Amer. Meteor. Soc., 354–355.

——, 2000: Comments on ''Development and evaluation of a convective scheme for use in climate models.'' *J. Atmos. Sci.,* **57,** 3686–3686.

——, 2002: Nonsingular implementation of the Mellor–Yamada level 2.5 scheme in the NCEP Meso model. NCEP Office Note 437, 61 pp.

Kain, J. S., 2004: The Kain-Fritsch convective parameterization: An update. *J. Appl. Meteor.,* **43,** 170–181.

——, and J. M. Fritsch, 1990: A one-dimensional entraining/detraining plume model and its application in convective parameterization. *J. Atmos. Sci.,* **47,** 2784–2802.

——, and ——, 1993: Convective parameterization for mesoscale models: The Kain–Fritsch scheme. *The Representation of Cumulus Convection in Numerical Models, Meteor. Monogr.,* No. 24, Amer. Meteor. Soc., 165–170.

Kim, Y.-J., and A. Arakawa, 1995: Improvement of orographic gravity wave parameterization using a mesoscale gravity wave model. *J. Atmos. Sci.,* **52,** 1875–1902.

Klein, S. A., and D. L. Hartmann, 1993: The seasonal cycle of low stratiform clouds. *J. Climate,* **6,** 1587–1606.

Kreitzberg, C. W., and D. J. Perkey, 1976: Release of potential instability. Part I: A sequential plume model within a hydrostatic primitive equation model. *J. Atmos. Sci.,* **33,** 456–475.

Lauer, A., Y. Wang, V. T. J. Phillips, C. S. McNaughton, and R. Bennartz, 2009: Simulating marine boundary layer clouds over the eastern Pacific in a regional climate model with double-moment cloud microphysics. *J. Geophys. Res.,* **114,** D21205, doi:10.1029/2009JD012201.

Leung, L. R., Y.-H. Kuo, and J. Tribbia, 2006: Research needs and directions of regional climate modeling using WRF and CCSM. *Bull. Amer. Meteor. Soc.,* **87,** 1747–1751.

Louis, J. F., 1979: A parametric model of vertical eddy fluxes in the atmosphere. *Bound.-Layer Meteor.,* **17,** 187–202.

McCaa, J. R., and C. S. Bretherton, 2004: A new parameterization for shallow cumulus convection and its application to marine subtropical cloud-topped boundary layers. Part II: Regional simulations of marine boundary layer clouds. *Mon. Wea. Rev.,* **132,** 883–896.

Mellor, G. L., 1977: The Gaussian cloud model relations. *J. Atmos. Sci.,* **34,** 356–358.

——, and T. Yamada, 1982: Development of a turbulence closure model for geophysical fluid problems. *Rev. Geophys. Space Phys.,* **20,** 851–875.

Nakanishi, M., and H. Niino, 2004: An improved Mellor-Yamada level-3 model with condensation physics: Its design and verification. *Bound.-Layer Meteor.,* **112,** 1–31.

Nordeng, T. E., 1995: Extended versions of the convective parameterization scheme at ECMWF and their impact on the mean and transient activity of the model in the Tropics. ECMWF Research Department Tech. Memo. 206, 41 pp. [Available from European Centre for Medium-Range Weather Forecasts, Shinfield Park, Reading RG2 9AX, United Kindom.]

Pan, H.-L., and W.-S. Wu, 1995: Implementing a mass flux convective parameterization package for the NMC medium-range forecast model. NMC Office Note 409, 40 pp. [Available from NCEP/EMC, 5200 Auth Rd., Camp Springs, MD 20746.]

Park, S., and C. S. Bretherton, 2009: The University of Washington shallow convection and moist turbulence schemes and their impact on climate simulations with the Community Atmosphere Model. *J. Climate,* **22,** 3449–3469.

Pleim, J. E., 2007a: A combined local and nonlocal closure model for the atmospheric boundary layer. Part I: Model description and testing. *J. Appl. Meteor. Climatol.,* **46,** 1383–1395.

——, 2007b: A combined local and nonlocal closure model for the atmospheric boundary layer. Part II: Application and evaluation in a mesoscale meteorological model. *J. Appl. Meteor. Climatol.,* **46,** 1396–1409.

Randall, D. A., J. A. Abeles, and T. G. Corsetti, 1985: Seasonal simulations of the planetary boundary layer and boundary-layer stratocumulus clouds with a general circulation model. *J. Atmos. Sci.,* **42,** 641–676.

Rockel, B., E. Raschke, and B. Weyres, 1991: A parameterization of broad band radiative transfer properties of water, ice and mixed clouds. *Beitr. Phys. Atmos.,* **64,** 1–12.

Roeckner, E., and Coauthors, 1996: The atmospheric general circulation model ECHAM-4: Model description and simulation of present-day climate. Max-Planck Institute for Meteorology, Rep. 218, Hamburg, Germany, 90 pp.

Serpetzoglou, E., B. A. Albrecht, P. Kollias, and C. W. Fairall, 2008: Boundary layer, cloud, and drizzle variability in the southeast Pacific stratocumulus regime. *J. Climate,* **21,** 6191–6214.

Siebesma, A. P., and J. W. M. Cuijpers, 1995: Evaluation of parametric assumptions for shallow cumulus convection. *J. Atmos. Sci.,* **52,** 650–666.

——, and A. A. M. Holtslag, 1996: Model impacts of entrainment and detrainment rates in shallow cumulus convection. *J. Atmos. Sci.,* **53,** 2354–2364.

——, and Coauthors, 2003: A large eddy simulation intercomparison study of shallow cumulus convection. *J. Atmos. Sci.,* **60,** 1201–1219.

Simpson, J., 1971: On cumulus entrainment and one-dimensional model. *J. Atmos. Sci.,* **28,** 449–455.

——, and V. Wiggert, 1969: Models of precipitating cumulus towers. *Mon. Wea. Rev.,* **97,** 471–489.

Skamarock, W. C., J. B. Klemp, J. Dudhia, D. O. Gill, D. M. Barker, W. Wang, and J. G. Powers, 2008: A description of the Advanced Research WRF version 3. NCAR Tech. Note 475+STR, 113 pp.

Sommeria, G., and J. W. Deardorff, 1977: Subgrid-scale condensation in models of non-precipitating clouds. *J. Atmos. Sci.,* **34,** 344–355.

Tiedtke, M., 1983: The sensitivity of the time-mean large-scale flow to cumulus convection in the ECMWF model. *Proc. ECMWF Workshop on Convection in Large-Scale Models,* Reading, United Kingdom, ECMWF, 297–316.

——, 1989: A comprehensive mass flux scheme for cumulus parameterization in large-scale models. *Mon. Wea. Rev.,* **117,** 1779–1800.

Troen, I., and L. Mahrt, 1986: A simple model of the atmospheric boundary layer; sensitivity to surface evaporation. *Bound.-Layer Meteor.,* **37,** 129–148.

Wang, L., Y. Wang, A. Lauer, and S.-P. Xie, 2011: Simulation of seasonal variation of marine boundary layer clouds over the eastern Pacific with a regional climate model. *J. Climate,* **24,** 3190–3210.

Wang, Y., O. L. Sen, and B. Wang, 2003: A highly resolved regional climate model (IPRC-RegCM) and its simulation of the 1998 severe precipitation event over China. Part I: Model description and verification of simulation. *J. Climate,* **16,** 1721–1738.

——, S.-P. Xie, H.-M. Hu, and B. Wang, 2004a: Regional model simulations of marine boundary layer clouds over the southeast Pacific off South America. Part I: Control experiment. *Mon. Wea. Rev.,* **132,** 274–296.

——, H. Xu, and S.-P. Xie, 2004b: Regional model simulations of marine boundary layer clouds over the southeast Pacific off South America. Part II: Sensitivity experiments. *Mon. Wea. Rev.,* **132,** 2650–2668.

——, S.-P. Xie, B. Wang, and H. Xu, 2005: Large-scale atmospheric forcing by southeast Pacific boundary-layer clouds: A regional model study. *J. Climate,* **18,** 934–951.

——, L. Zhou, and K. P. Hamilton, 2007: Effect of convective entrainment/detrainment on simulation of tropical precipitation diurnal cycle. *Mon. Wea. Rev.,* **135,** 567–585.

Winker, D. M., M. A. Vaughan, A. Omar, Y.-X. Hu, K. A. Powell, Z. Liu, W. H. Hunt, and S. A. Young, 2009: Overview of the CALIPSO mission and CALIOP data processing algorithms. *J. Atmos. Oceanic Technol.,* **26,** 2310–2323.

Wolfe, D. E., V. Ghate, and L. Bariteau, cited 2006: 2006 WHOI/NOAA stratus 2006: Field program on the NOAA Research Vessel Ronald H. Brown. NOAA/Earth System Research Laboratory, 34 pp. [Available online at ftp://ftp1.esrl.noaa.gov/psd3/cruises/STRATUS_2006/RHB/Scientific_analysis/PSD_data_sum_stratus06_v5.pdf.]

Wyant, M. C., and Coauthors, 2010: The PreVOCA experiment: Modeling the lower troposphere in the southeast Pacific. *Atmos. Chem. Phys.,* **10,** 4757–4774.

Xu, H., S.-P. Xie, Y. Wang, and R. J. Small, 2005: Effects of central American Mountains on the eastern Pacific winter ITCZ and moisture transport. *J. Climate,* **18,** 3856–3873.

Xu, K.-M., and D. A. Randall, 1996: A semiempirical cloudiness parameterization for use in climate models. *J. Atmos. Sci.,* **53,** 3084–3102.

Yanai, M., S. Esbensen, and J.-H. Chu, 1973: Determination of bulk properties of tropical cloud clusters from large-scale heat and moisture budgets. *J. Atmos. Sci.,* **30,** 611–627.